The Grid-Connected Inverter Stability Enhancement Control Based on Impedance Instability Region Elimination

Zhengqi Sui, Qiuye Sun, *Senior Member, IEEE*, Rui Wang, *Senior Member, IEEE*,
Dashuang Li, *Student Member, IEEE*, and Peng Wang, *Fellow, IEEE*

***Abstract*—The weak grid and high phase-locked loop (PLL) bandwidth can easily cause instability issues in the grid-connected Inverter (GCI) system. The present methods mainly enhance system stability by increasing the magnitude and phase of the GCI output impedance, but it cannot completely eliminate the "negative impedance" behavior of the GCI. It means that there is still a risk of instability in the system. Therefore, this article aims to propose a more general stability analysis method, revealing the instability conditions under negative impedance and providing a new insight for stability analysis and control strategy design. First, this article considers the broadband oscillation characteristics exhibited during GCI instability and proposes a new stability analysis method. This method indicates that the system instability is caused by the interaction between fundamental voltage and nonfundamental voltage. This interaction can exacerbate the oscillation of system voltage, ultimately leading to instability issues. This method provides a clear physical explanation for the mechanism of system instability. Second, a new impedance-based stability discrimination method is obtained, determining the conditions for GCI instability. This method can provide a clearer explanation of the present instability phenomena. Then, a compensation method based on *q*-axis voltage is proposed. This method achieves complete decoupling between the GCI impedance and voltage, effectively eliminating the instability region. Compared with existing methods, the method proposed can better ensure the stability of GCI under weak grid and high PLL bandwidth. Finally, the effectiveness of the proposed methods is verified through simulations and experiments.**

***Index Terms*—Compensation-based control, grid-connected inverter (GCI), instability conditions, stability analysis, stability enhancement.**

I. INTRODUCTION

WITH the increasing demand for electricity and growing environmental pressures, renewable energy sources are being integrated into the grid through power electronics converters [1]. Among them, the grid-connected inverters (GCIs) have been widely applied due to their simple control structure and efficient power output [2]. However, due to the large line impedance [3] and the need for high transmission power [4], the system exhibits weak grid characteristics [5]. The GCIs are prone to instability issues. Therefore, it is of great significance to study the stability of the GCIs under weak grid and propose corresponding methods for enhancing stability.

The impedance-based approaches are the important method for analyzing the stability of GCI system [6]. The authors in [7] suggested that the phase-locked loop (PLL) can introduce a positive feedback loop into the system, leading to negative impedance behavior and potential instability. In addition, [7] noted that a larger PLL bandwidth results in a broader frequency range of negative impedance, making the system more prone to instability. The authors in [8] proposed that weaker grid conditions (that is, the higher line impedance and greater transmission power) make GCI more susceptible to instability. However, the conclusions drawn require point-by-point evaluations of the system stability, leading to numerical conclusions. The authors in [9] analyzed the causes of common instability phenomena by plotting multiple Nyquist curves. This method is challenging for assessing all situations individually and obtaining universal conclusions. Meanwhile, this method attributes instability to the Nyquist curve to encircle $(-1, j0)$ or the magnitude-frequency curve to intersect in the negative impedance frequency region. But it is difficult to explain why weaker grid conditions and larger PLL bandwidth make it more likely for this phenomenon to occur. The authors in [10] also pointed out that existing impedance methods fail to connect the instability issue with the physical properties of actual power systems. Therefore, it is essential to propose a more general stability analysis method to identify overarching patterns and provide clear physical explanations for existing instability phenomena.

Furthermore, in order to enhance the stability of GCIs in weak grid, design-oriented methods have been proposed [11], [12], [13], [14]. The authors in [11] and [12] presented a simple and effective stability enhancement method by reducing the PLL bandwidth. However, a slower PLL response negatively impacts the dynamic performance of the PLL, which is detrimental to high-performance current control and the fault ride-through

---

Received 14 November 2024; revised 24 December 2024 and 5 February 2025; accepted 6 March 2025. Date of publication 11 March 2025; date of current version 14 April 2025. This work was supported by the National Natural Science Foundation of China under Grant 5247072151, Grant 52307194, and Grant 62433013. Recommended for publication by Associate Editor A. Kuperman. *(Corresponding author: Qiuye Sun.)*

Zhengqi Sui, Qiuye Sun, Rui Wang, and Dashuang Li are with the College of Information Science and Engineering, Northeastern University, Shenyang 110819, China (e-mail: 2110260@stu.neu.edu.cn; sunqiuye@ise.neu.edu.cn; wangrui@ise.neu.edu.cn; 2210276@stu.neu.edu.cn).

Peng Wang is with the School of Electrical and Automation Engineering, Nanjing Normal University, Nanjing 210023, China (e-mail: epwang@ntu.edu.sg).

Color versions of one or more figures in this article are available at https://doi.org/10.1109/TPEL.2025.3550310.

Digital Object Identifier 10.1109/TPEL.2025.3550310

capability of GCIs [13]. The authors in [13] and [14] provided guidelines for selecting the controller parameters for both the PLL and current controller. However, the parameter design process for them must be considered simultaneously, indicating a strong coupling between PLL and current controller parameters. This coupling increases the complexity of the system design.

Compared with design-oriented methods, the methods based on modifying control structure have been extensively researched [15], [16], [17], [18], [19]. This method is divided into two categories: One is based on modifying the PLL structure, and the other is the current loop compensation control. The authors in [15] proposed a decoupling strategy between the PLL and grid impedance, making the PLL bandwidth independent of system stability and avoiding instability caused by the PLL. However, this technique relies on online grid impedance measurements, which reduces its reliability. The authors in [16] introduced a PLL based on a constant coupling effect, but the coupling term is related to the output voltage/current, and variations in voltage/current affect the degree of coupling. At the same time, the design process of these methods is complex and the relevant parameters are difficult to obtain. On the other hand, compensation-based control methods aim to eliminate the coupling between the impedance and the PLL, improving the GCI impedance phase and magnitude while reducing the negative impedance region. The authors in [17] proposed introducing a *q*-axis voltage compensation term on the *q*-axis. The authors in [18] suggested introducing a *d*-axis voltage compensation term on the *d*-axis and a *q*-axis voltage compensation term on the *q*-axis, respectively. The authors in [19] proposed introducing *q*-axis voltage compensation terms on both the *d*-axis and *q*-axis. However, based on the simulation results from the above references, these methods cannot completely eliminate the negative impedance. According to the existing stability analysis results, this implies that the compensated GCI still carries the risk of instability. Therefore, it is necessary to clarify the instability conditions of the GCI under negative impedance, and further propose corresponding stability enhancement strategies to improve the stability of GCI under weak grid and high PLL bandwidth.

In addition, GCI is a typical time-varying system. Due to external disturbances and the fluctuation of renewable energy output, its operating point continuously changes [20]. The authors in [21] proposed a GCI impedance model based on variable operating point (VOP), which can describe the dynamic characteristics of the system more comprehensively and accurately. Therefore, this article analyzes the instability mechanism of GCI based on the VOP impedance model and proposes an effective compensation method.

The main advantages of this article are as follows.

1) A new stability analysis method is proposed based on the variation characteristics of the GCI VOP impedance with point of common coupling (PCC) voltage. This method analyzes the dynamic interaction process between the fundamental voltage and nonfundamental voltage under small disturbances, thus explaining the instability mechanism of GCI. In contrast to the traditional impedance-based analysis, this approach considers the broadband oscillation characteristics of GCI instability from a basic circuit perspective, providing a clearer physical explanation for the instability mechanism of GCI.

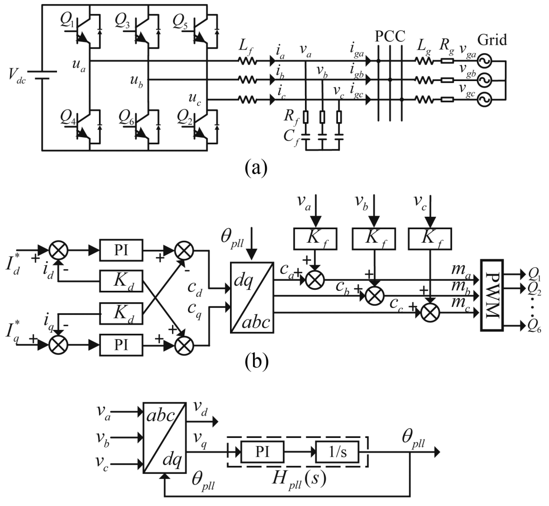

(a)
(b)
(c)

Fig. 1. Topology and control scheme of the GCI. (a) Topology of the GCI. (b) Control scheme of the GCI. (c) The control structure of the PLL.

2) Based on the stability analysis method, a straightforward stability discrimination region is proposed, where only the synthetic impedance phase is used to accurately assess the stability of GCI. The method identifies the instability conditions when the GCI exhibits negative impedance and provides a clear explanation for existing instability phenomena, with conclusions that are more generally applicable. It eliminates the need to derive summary rules through point-by-point plotting of the Nyquist curves or Bode plots.

3) A simple compensation control method based on *q*-axis voltage is proposed. This method achieves complete decoupling between the GCI output impedance and voltage, thereby avoiding the emergence of instability regions. Compared with existing methods, this method significantly enhances the performance of the GCI under weak grid and high PLL bandwidth.

The rest of this article is organized as follows. In Section II, based on the VOP impedance model of the GCI, the change law of impedance with the PCC voltage is found. Furthermore, a new stability analysis method is proposed, further obtaining a new stability discriminant region and explaining the instability mechanism of GCI under weak grid and high PLL bandwidth in Section III. In Section IV, a *q*-axis voltage compensation control method is proposed. In Sections V and VI, the simulation and experimental results are separately provided to validate the effectiveness of the method proposed. Finally, Section VII concludes this article.

II. VARIABLE OPERATING POINT IMPEDANCE CHARACTERISTICS OF THE GCI

Fig. 1 illustrates the topology and control scheme of the GCI. V_{dc} is the dc-side voltage of the GCI; u_a, u_b and u_c are the inner electric potentials; i_a, i_b, and i_c are the output currents; v_a, v_b, and v_c are the output terminal voltages; L_f, C_f, and R_f are the filter inductance, filter capacitance, and damping resistance, respectively; L_g and R_g are the line inductance and resistance of the grid, respectively; v_{ga}, v_{gb}, and v_{gc} are the grid voltages; i_{ga}, i_{gb}, and i_{gc} are the grid-connected currents; c_{abc} is the modulation signal. The subscripts "d" and "q" represent the components of variables in the *d*-axis and *q*-axis, respectively. The superscript "$*$" indicates the reference value of the variable.

A. Control Scheme of the GCI

The GCI adopts closed-loop control of the inductor current, as shown in Fig. 1(b). The control equations of the current loop are shown as

$$c_d = (I_d^* - i_d)H_i(s) - K_d i_q \tag{1}$$

$$c_q = (I_q^* - i_q)H_i(s) + K_d i_d \tag{2}$$

where $H_i(s) = k_{pi} + k_{ii}/s$; k_{pi} and k_{ii} are the proportional and integral coefficients of the current loop PI controller, respectively; K_d is the decoupling coefficient.

The rotational reference angle θ_{pll} is generated by the PLL as shown in Fig. 1(c). The relationship between $\Delta\theta$ and v_q can be obtained as

$$\Delta\theta = H_{pll}(s)v_q \tag{3}$$

where $H_{pll}(s) = (k_p + k_i/s)/s$; k_p and k_i are the proportional and integral coefficients of the PLL PI controller, respectively.

B. VOP Impedance Modeling of the GCI

Based on the harmonic linearization method, the detailed modeling process of the VOP impedance model has been derived in [21]. It is provided in Appendix A. The introduction of V_1 and I_1 are analyzed. The impedance model of the GCI considering VOPs can be obtained as

$$Z_{gcip}(s) = \frac{sL_f + \frac{V_{dc}}{2}(H_i(s-j2\pi f_1) - jK_d)G_i(s)}{1 - \frac{V_{dc}}{2}K_f G_v(s) - \frac{V_{dc}}{4}\frac{T(s-j2\pi f_1)}{V_1} G_v(s)(H_i(s-j2\pi f_1) - jK_d)I_1 e^{j\phi_{i1}}} \tag{4}$$

$$Z_{gcin}(s) = \frac{sL_f + \frac{V_{dc}}{2}(H_i(s+j2\pi f_1) + jK_d)G_i(s)}{1 - \frac{V_{dc}}{2}K_f G_v(s) - \frac{V_{dc}}{4}\frac{T(s+j2\pi f_1)}{V_1} G_v(s)(H_i(s+j2\pi f_1) + jK_d)I_1 e^{-j\phi_{i1}}} \tag{5}$$

where V_1 is the amplitude of the fundamental PCC voltage; f_1 is the fundamental frequency; I_1 is the amplitude of the fundamental current; ϕ_{i1} is the initial phase angle of the fundamental current; $T(s) = V_1 H_{pll}(s)/[1 + V_1 H_{pll}(s)]$; $G_{v/i}(s) = e^{-Ts}(1 - e^{-Ts})/[(Ts)(1 + s/\omega_{v/i})]$ is the sampling function, which simulates the sampling delay, PWM delay and sampling low-pass filter; T is the sampling period, $\omega_{v/i}$ is the cutoff angle frequency of the low-pass filter; K_f is the voltage feedforward coefficient.

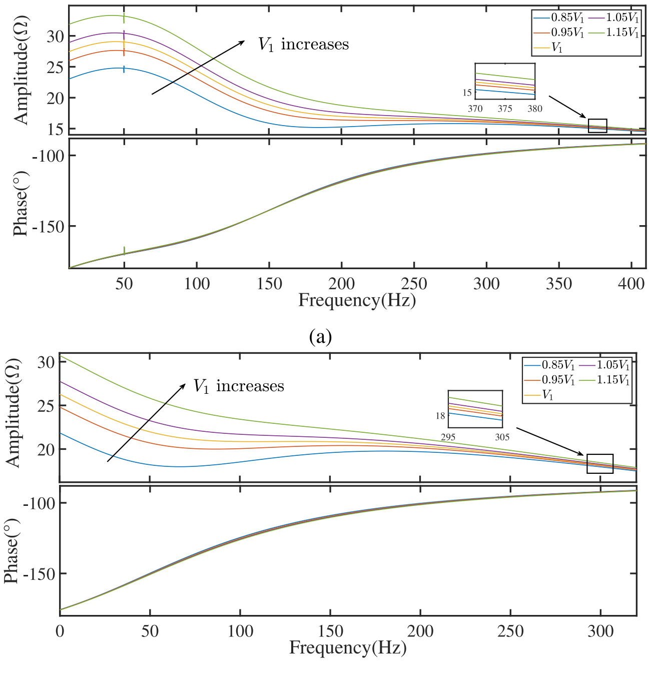

(a)

(b)

Fig. 2. GCI impedance variation with V_1 when the PLL controller is set to $3.71 + 2145/s$ and the current controller is set to $0.074 + 0.2467/s$. (a) Positive sequence impedance. (b) Negative sequence impedance.

The vector relationship between the output current and the grid-connected point voltage can be shown as

$$\mathbf{V}_1 = (R_g + j2\pi f_1 L_g)\mathbf{I}_1 + \mathbf{V}_g \tag{6}$$

where $\mathbf{V}_1$, $\mathbf{I}_1$, and $\mathbf{V}_g$ are PCC voltage vector, output current vector, and grid voltage vector, respectively.

C. GCI Impedance Model Law Discovery

For the purpose of subsequent theoretical analysis, the filter inductor is considered as the part of the GCI output impedance. Therefore, the output impedance of the GCI is defined as

$$Z_{1p}(s) = Z_{gcip}(s)//(R_f + 1/sC_f) \tag{7}$$

$$Z_{1n}(s) = Z_{gcin}(s)//(R_f + 1/sC_f) \tag{8}$$

where $Z_{1p}(s)$ and $Z_{1n}(s)$ are the positive and negative output sequence impedance of the GCI, respectively.

Considering the variability of the GCI operating point, and through an extensive series of simulation experiments, this article identifies a new characteristic of the GCI impedance model: Within the negative resistance-capacitive frequency range, the magnitude of the equivalent impedance decreases with decreasing PCC voltage V_1 or increasing output current I_1, while the phase remains unchanged, as shown in Figs. 2 and 3. The positive sequence impedance range of the GCI is from 9 to 410 Hz, while the negative sequence impedance range is from 0 to 325 Hz. The system topology is depicted in Fig. 1 and the system parameters are shown in Table I.

According to the impedance-based approaches, when the impedance of the GCI exhibits negative resistance-capacitance

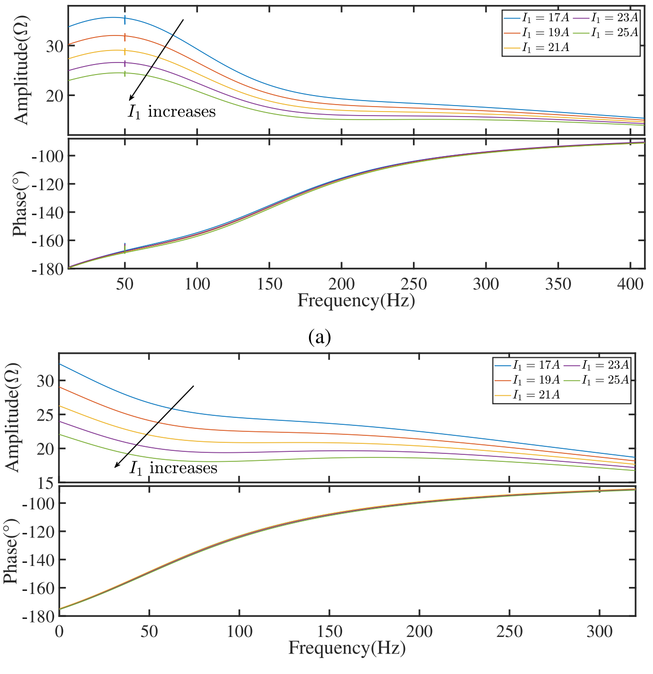

(a)

(b)

Fig. 3. GCI impedance variation with I_1 when the PLL controller is set to $3.71 + 2145/s$ and the current controller is set to $0.074 + 0.2467/s$. (a) Positive sequence impedance. (b) Negative sequence impedance.

TABLE I
PARAMETERS OF GCI

Parameter	Symbol	Value
DC voltage source	V_{dc}	700 V
Grid voltage	V_g	311 V
Switching frequency	f_{sw}	20 kHz
Current PI controller	k_{pi}/k_{ii}	0.074/0.2467
PLL PI controller	k_p/k_i	3.71/2145
Voltage feedforward coefficient	K_f	0.0029
Decoupling coefficient	K_d	0.942
Filter inductance	L_f	3 mH
Filter capacitor	C_f	20 μF
Filter resistance	R_f	1.5 Ω

characteristics, the system is prone to instability. Therefore, this article aims to combine the negative impedance characteristics of the GCI and the impedance variation with V_1 to elucidate the reason for system instability occurrences.

D. Theoretical Proof of the Impedance Variation Law of GCI.

In order to demonstrate the generality of the conclusions obtained, this section will provide a specific theoretical analysis process.

Based on the vector synthesis relationship between voltage disturbance and current response, [7] analyzes the relationship between the magnitude of q-axis impedance and current within the bandwidth of the PLL. This article will analogize the theoretical proof process used in [7] and analyze the reasons for the variation of GCI output impedance with voltage/current. The following analysis will take the case of positive sequence impedance as an example. Similarly, the same conclusion can be drawn for negative sequence impedance.

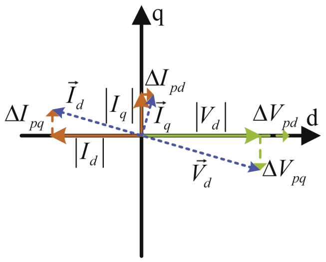

Fig. 4. Schematic diagram of the vector synthesis relationship between positive sequence voltage disturbance and current response.

As shown in Fig. 4, when a positive sequence voltage disturbance V_p is injected into the GCI, it can be decomposed into d-axis voltage disturbance ΔV_{pd} and q-axis voltage disturbance ΔV_{pq}. The corresponding positive sequence current response can be decomposed into d-axis response ΔI_{pd} and q-axis response ΔI_{pq}. It is important to note that, according to [22], the generation of the current response is mainly influenced by the q-axis voltage disturbance, as the PLL needs to track the phase through the q-axis voltage.

Within the bandwidth of the PLL, the q-axis voltage disturbance causes the voltage vector to shift from alignment with the d-axis to $\vec{V}_d$. Due to the action of the PLL, the current vector will rotate to maintain synchronization with the voltage vector, causing $|I_d|$ to shift from alignment with the d-axis to $\vec{I}_d$, as shown in Fig. 4. Thus, according to the theory of similar triangles, it can be concluded that

$$\frac{|I_d|}{|V_d|} \approx \frac{|\Delta I_{pq}|}{|\Delta V_{pq}|}. \tag{9}$$

Similarly, within the bandwidth of the PLL, for the d-axis current response, the current vector will rotate to maintain a perpendicular alignment with the voltage vector, causing $|I_q|$ to shift from alignment with the q-axis to $\vec{I}_q$, as shown in Fig. 4. Therefore, it can be concluded that

$$\frac{|I_q|}{|V_d|} \approx \frac{|\Delta I_{pd}|}{|\Delta V_{pq}|}. \tag{10}$$

Therefore, combining (9), (10), and the calculation principles of positive sequence impedance

$$\begin{aligned} Z_{gcip} &= \frac{|\Delta V_{pd}| + j|\Delta V_{pq}|}{|\Delta I_{pd}| + j|\Delta I_{pq}|} \\ &\approx \frac{|\Delta V_{pd}| + j|\Delta V_{pq}|}{\frac{|I_q|}{|V_d|}|\Delta V_{pq}| + j\frac{|I_d|}{|V_d|}|\Delta V_{pq}|} \\ &= |V_d| \frac{|\Delta V_{pd}| + j|\Delta V_{pq}|}{(|I_d| - j|I_q|)j|\Delta V_{pq}|} \\ &= -\frac{j|V_d|V_p}{|I_1|e^{-j\phi_{i1}}|\Delta V_{pq}|}. \end{aligned} \tag{11}$$

According to the calculation results in (11), it can be concluded that within the PLL bandwidth, the output impedance of GCI is negative impedance, and changes in voltage magnitude and current magnitude have little effect on the phase of GCI output impedance. They primarily affect the impedance magnitude. The current magnitude is inversely proportional to the impedance magnitude, while the voltage magnitude is directly proportional to the impedance magnitude. Similarly, this theory also applies to the analysis of the variation law of negative sequence impedance Z_{gcin}. Furthermore, after the GCI impedance is connected in parallel with the filtering capacitor, the GCI output impedance is primarily determined by Z_{gcip} and Z_{gcin} in (7) and (8) within the PLL control bandwidth, which means that Z_{1p} and Z_{1n} exhibit the same variation law as Z_{gcip} and Z_{gcin}.

III. STABILITY ANALYSIS OF THE GCI

A. Discussion on Stability Analysis Approach

Some researchers analyze the instability conditions of GCI when the output impedance is negative from the perspective of fundamental circuits. In [23], it is proposed that the combination of negative resistance with other components in the system can form a negative resistance oscillator under certain conditions. In [24], it was proposed that when GCI exhibits negative resistance in absolute terms capable of overcoming the grid-side resistance, it may result in electrical oscillations between the grid inductance and equivalent capacitance. However, the presence of negative resistance inevitably leads to negative damping within the entire control system, potentially causing system oscillations, without the necessity for the system to undergo series or parallel resonance. At the same time, when GCI instability occurs, it usually manifests as broadband oscillations [25]. These types of methods struggle to explain the cause of the oscillations in the GCI output signals.

Therefore, to obtain the instability conditions of GCI under negative impedance, this article draws an analogy to the analytical approach used in static rotor angle stability analysis to determine the stable operating range of the rotor angle. In rotor angle stability analysis, the stability and instability intervals of the rotor angle are analyzed using the $P_e - \delta$ curve (i.e., $P_e = P_{\max}\sin(\delta)$.) [26]. In this method, the difference between electrical power and mechanical power is utilized to assess the acceleration (or deceleration) process of the rotor angle, leading to the identification of the stable range $[0, \pi/2]$ and the unstable range $[\pi/2, \pi]$. This process utilizes the interaction relationship between active power and rotor angle.

However, unlike rotor angle stability analysis, which is based on the fundamental frequency, the broadband oscillation phenomenon of GCI is characterized by significant oscillation amplitudes in nonfundamental signals. The fundamental signals output interacts with nonfundamental signals, ultimately leading to instability issues [25]. In addition, the stability classification article published by IEEE/GICRE in 2020 mentions that "in practice, small disturbance instability is characterized by the system passing through a series of operating points until the "final" event pushes the system into an unstable state" [27]. Therefore, the stability analysis of GCI needs to fully consider the interaction between fundamental and nonfundamental signals under small disturbances.

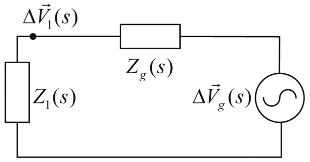

Fig. 5. Equivalent circuit model of the GCI system.

Based on this analytical approach, this article establishes a superposition model for the fundamental voltage and nonfundamental voltage at the grid connection point. By integrating the impedance variation patterns identified in Section II, the evolution process of the PCC voltage under disturbances is analyzed, thereby providing a clear physical explanation for this issue and deriving the instability conditions when GCI exhibits negative impedance.

B. Stability Mechanism Analysis

The authors in [28] pointed out that for GCI grid-connected system, GCI can be equivalent to the form of impedance. Therefore, the equivalent circuit of GCI system under disturbance can be obtained in Fig. 5, where $\Delta\vec{V}_g(s)$ is the small external perturbation, $Z_g(s)$ is the line impedance, and $Z_1(s)$ is the GCI equivalent impedance.

According to Fig. 5, the PCC voltage disturbance can be expressed as

$$\Delta\vec{V}_1(s) = \frac{Z_1(s)}{Z_1(s) + Z_g(s)}\Delta\vec{V}_g(s). \tag{12}$$

Then, the PCC voltage vector can be expressed as the sum of the fundamental voltage vector and the disturbance voltage vector, which can be shown in (13). This expression has also been applied in [7]

$$\begin{aligned}\vec{V}_s &= \vec{V}_1 + \Delta\vec{V}_1(s)\\ &= \vec{V}_1 + \frac{Z_1(s)}{Z_1(s) + Z_g(s)}\Delta\vec{V}_g(s)\\ &= \vec{V}_1 + \Delta\vec{V}_g(s) + \left(-\frac{Z_g(s)}{Z_1(s) + Z_g(s)}\right)\Delta\vec{V}_g(s). \end{aligned} \tag{13}$$

According to (13), we can define

$$A = A_1 + A_2 \tag{14}$$

where $A = \vec{V}_s$, $A_1 = \vec{V}_1 + \Delta\vec{V}_g(s)$ can be considered as a constant, $A_2 = -\frac{Z_g(s)}{Z_1(s)+Z_g(s)}\Delta\vec{V}_g(s)$.

Based on (13) and (14), it can be observed that the magnitude of A is jointly determined by the magnitudes of A_1 and A_2. The magnitude of A can be approximately represented by V_1, which is a constant value under undisturbed conditions. After being subjected to disturbances, the variation of V_1 is shown in Fig. 6. This variation includes both increasing and decreasing states. Furthermore, according to the conclusions obtained in Section II, the change in A will affect the change in $Z_1(s)$, which in

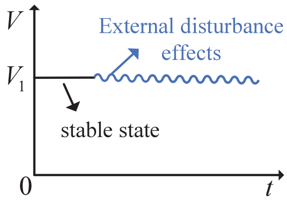

Fig. 6. Schematic diagram of fundamental signal superimposed with disturbance signal.

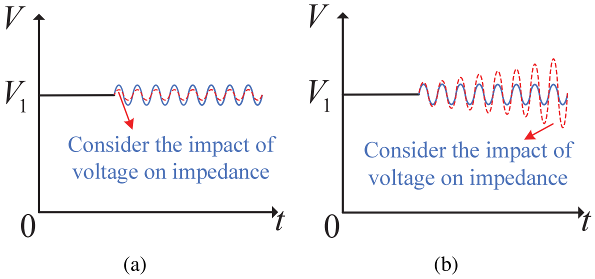

(a) (b)

Fig. 7. Illustration of PCC voltage variations after being disturbed. (a) Stable state. (b) Unstable state.

turn influences the magnitude change of A_2. If A increases, the magnitude of A_2 can decrease to suppress the increase of A; conversely, if A decreases, the magnitude of A_2 can increase to suppress the decrease of A. Then, the system can maintain stability. In this case, the variation of A is illustrated by the red line in Fig. 7(a). It oscillates with fluctuations slightly below the amplitude of the original disturbance. Once the disturbance subsides, the voltage can return to the original operating point. On the other hand, if the magnitudes of A and A_2 both increase or decrease simultaneously, the change in A cannot be suppressed. This further impacts the variation of A_2, creating a vicious cycle. Under small disturbances, A will continuously increase or decrease, leading to instability issues. In this case, the variation of A is illustrated by the red line in Fig. 7(b). A gradually diverges in oscillation until instability occurs.

Therefore, studying the stability issues of GCI can be transformed into analyzing how the magnitude of $-Z_g(s)/(Z_1(s)+Z_g(s))$ changes with variations in voltage. Since $Z_g(s)$ does not change with voltage variations, it is sufficient to study how $-1/(Z_1(s)+Z_g(s))$ changes with V_1.

C. Analysis of Stable and Unstable Regions

We assume that the system experiences positive sequence (or negative sequence) disturbance with a frequency of ω_1. According to the model established by (13), at this frequency, the output impedance of GCI is $Z_1(\omega_1)$, the phase of $Z_1(\omega_1)$ is $\theta_1(\omega_1)$, the line impedance is $Z_g(\omega_1)$, the system impedance $Z_1(\omega_1)+Z_g(\omega_1)$ is $Z(\omega_1)$, the phase of $Z(\omega_1)$ is $\theta(\omega_1)$. Since ω_1 can be expressed as any frequency within the negative impedance frequency band, this analysis method can be used to analyze the stability at any frequency within the negative impedance frequency band.

Due to $Z_1(\omega_1)$ is negative resistance-capacitance and $Z_g(\omega_1)$ is positive resistance-inductance ($Z_g(\omega_1)=R_g+j\omega_1 L_g$), $\theta_1(\omega_1)$ lies within $[-\pi,-\pi/2]$ and the phase of $Z_g(\omega_1)$ lies within $[0,\pi/2]$. Then, the phase of $Z(\omega_1)$(that is $\theta(\omega_1)$) may potentially exist at various positions within $[-\pi,\pi]$. It is necessary to partition $[-\pi,\pi]$ and conduct independent analysis. In addition, since both increasing or decreasing the PCC voltage yield the same analytical results, this article uses an increase in PCC voltage as an example to discuss the stability within various interval.

Fig. 8 illustrates the variation of $Z(\omega_1)$ when the PCC voltage increases. The principle used is that the perpendicular segment in a triangle is the shortest. That is, when $Z(\omega_1)$ is perpendicular to $Z_1(\omega_1)$, $Z(\omega_1)$ is the shortest. Therefore, each region in Fig. 8 is divided based on the straight line on which $Z_1(\omega_1)$ lies and the straight line on which the perpendicular of $Z_1(\omega_1)$ lies. The subinterval corresponds to the interval where $\theta(\omega_1)$ is located. Regardless of the position of $Z_1(\omega_1)$ within $[-\pi,-\pi/2]$, as long as $\theta(\omega_1)$ is within the corresponding interval, the same analysis result can be obtained.

When A increases due to an external disturbance, the amplitude of $Z_1(\omega_1)$ will increase while the phase will remain constant. According to Fig. 8(a), (b), (c), and (h), when $\theta(\omega_1)$ is located at $[0,\theta_1(\omega_1)+3\pi/2]$ or $[\theta_1(\omega_1)+\pi/2,0]$, the magnitude of $Z(\omega_1)$ will decrease. Then, the magnitude of $(-1/Z(\omega_1))$ will increase. According to (14), the change in the amplitude of A_2 will be unable to suppress the increase of A, leading to a vicious cycle and causing instability issues. Similarly, when A decreases, the change in the amplitude of A_2 will also decrease. It cannot suppress the decrease of A. Therefore, $[0,\theta_1(\omega_1)+3\pi/2]$ and $[\theta_1(\omega_1)+\pi/2,0]$ are the destabilization intervals.

According to Fig. 8(d)–(g), when $\theta(\omega_1)$ is located at $[\theta_1(\omega_1)+3\pi/2,\pi]$ or $[-\pi,\theta_1(\omega_1)+\pi/2]$, the magnitude of $Z(\omega_1)$ will increase. Then, the magnitude of $(-1/Z(\omega_1))$ will decrease. According to (14), the change in the amplitude of A_2 can suppress the increase of A. Then, the system can maintain stability. Similarly, when A decreases, the change in the amplitude of A_2 will increase. It can also suppress the decrease of A. Therefore, $[\theta_1(\omega_1)+3\pi/2,\pi]$ and $[-\pi,\theta_1(\omega_1)+\pi/2]$ are the stabilization intervals.

According to the above analysis process, it can be concluded that when the system is disturbed, the amplitude of the fundamental voltage fluctuates, which in turn affects the nonfundamental voltage. If the fundamental voltage and the nonfundamental voltage exhibit opposite trends, they will counteract the changes of each other. Changes in the PCC voltage will be suppressed, keeping the system stable. Conversely, if the fundamental and nonfundamental voltage change in the same direction, the PCC voltage will continue to shift along this trend, causing the fundamental and nonfundamental voltage to reinforce the changes of each other. This cyclic process will exacerbate the oscillation of the PCC voltage, ultimately leading to instability issues. Based on the analysis results, a new stability discrimination region is further obtained, as shown in Fig. 9. It only uses the synthetic impedance phase to assess stability. The dividing line is the vertical line corresponding to $Z_1(s)$. When

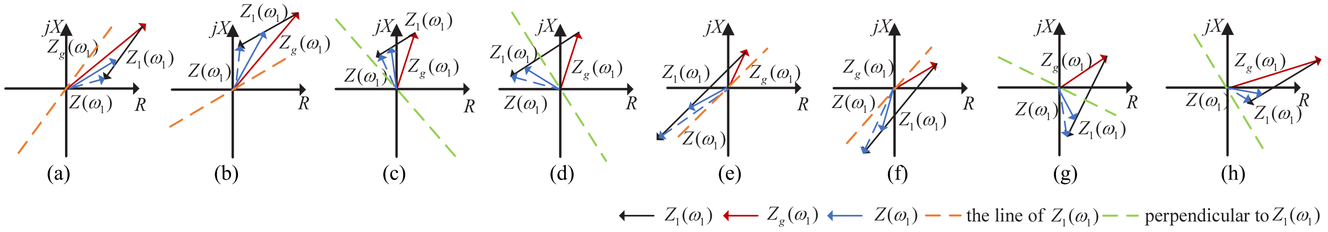

Fig. 8. Schematic diagram of $Z(\omega_1)$ changing with V_1. (a) $\theta(\omega_1) \in [0, \theta_1(\omega_1) + \pi]$. (b) $\theta(\omega_1) \in [\theta_1(\omega_1) + \pi, \pi/2]$. (c) $\theta(\omega_1) \in [\pi/2, \theta_1(\omega_1) + 3\pi/2]$. (d) $\theta(\omega_1) \in [\theta_1(\omega_1) + 3\pi/2, \pi]$. (e) $\theta(\omega_1) \in [-\pi, \theta_1(\omega_1)]$. (f) $\theta(\omega_1) \in [\theta_1(\omega_1), -\pi/2]$. (g) $\theta(\omega_1) \in [-\pi/2, \theta_1(\omega_1) + \pi/2]$. (h) $\theta(\omega_1) \in [\theta_1(\omega_1) + \pi/2, 0]$.

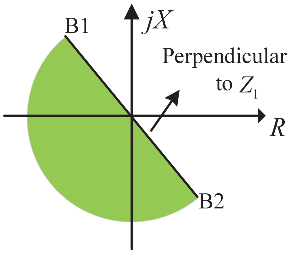

Fig. 9. New impedance-based stability discrimination region: the green region is stable, the remaining is unstable.

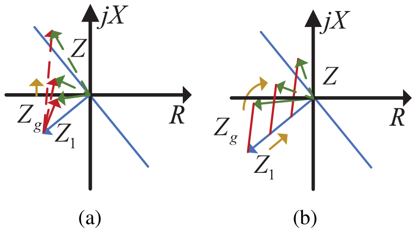

Fig. 10. Diagram of Z changes with Z_g or I_1. (a) The variation of Z with the increase of Z_g. (b) The variation of Z with the increase of I_1.

the phase of the synthesized impedance $Z(s)$ lies in the green region, the system will remain stable; on the contrary, the system will be destabilized.

D. Explanation of Common Instability Phenomena in GCI

1) The Higher the Line Impedance, the Worse the System Stability: When the line impedance increases, as shown in Fig. 10(a), it causes the synthesized impedance Z to cross the negative half of the x-axis and gradually enter the instability region, thus leading to the occurrence of instability phenomena.

2) Higher the Output Power, the Worse the System Stability: Increasing the output power of the GCI will result in an increase in its output current. Based on Fig. 3, it can be observed that the magnitude of the GCI equivalent impedance decreases with the growth of the output current, while the phase remains constant. Therefore, according to Fig. 10(b), as the current increases, the synthesized impedance Z will gradually approach the negative half of the x-axis and may potentially enter the instability region, thus leading to the occurrence of instability phenomena.

3) Higher the PLL Bandwidth, the Worse the System Stability: The larger the bandwidth of the PLL, the greater the negative impedance frequency range of Z_1. This will lead to an increase in the magnitude corresponding to the line impedance, making it similar to the situation depicted in Fig. 10(a), which can easily drive the system synthetic impedance into the instability region.

The instability of GCI under weak grid and high PLL bandwidth is caused by a decrease in the equivalent impedance of GCI or an increase in the line impedance, which results in the synthesized impedance Z entering the instability region. The emergence of the instability region is due to the fact that within this range, changes in PCC voltage cannot be suppressed. Therefore, if the equivalent impedance of the GCI remains constant with changes in voltage, it can effectively prevent the appearance of the instability region and thereby enhance system stability.

IV. STABILITY ENHANCEMENT METHOD FOR GCI

A. Compensation Method Based on Q-Axis Voltage

Based on the analysis and conclusions drawn in the preceding sections, this section introduces a compensation-based control method that ensures the output impedance of GCI remains constant regardless of changes in voltage. This effectively enhances the stability of GCI under weak grid and high PLL bandwidth.

Observing (4) and (5), the variation in GCI output impedance with changes in voltage is due to the presence of V_1 in its denominator. If it is possible to make the coefficient of V_1 equal to zero, GCI output impedance can remain constant. The coefficient of V_1 includes $T(s)$, $H_i(s)$, $G_v(s)$, and I_1, with $G_v(s)$ and I_1 being inherent system variables/parameters that cannot be altered. Therefore, the most direct approach would be to design the parameters of $T(s)$ and $H_i(s)$ so that their product in the frequency domain equals zero. However, simultaneously designing all four parameters is quite difficult. At the same time, the coefficient of V_1 is introduced due to the PLL, which is related to the q-axis voltage [19]. Based on this, this article proposes to superimpose a q-axis voltage compensation component on the current loop control to cancel the perturbation component due to the grid impedance acting with PLL and at the same time, make the coefficient of V_1 become 0. Therefore, the compensation terms for the d-axis and q-axis can be obtained as

$$G_{1d}(s) = \frac{T(s)(I_d K_d - I_q H_i(s))}{V_1(T(s) - 1)} \tag{15}$$

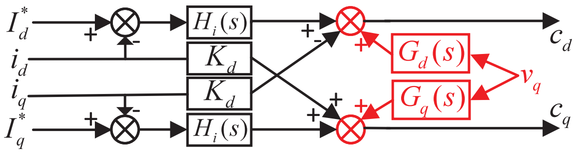

Fig. 11. Current loop with added compensation control.

$$G_{1q}(s) = -\frac{T(s)(I_d H_i(s) + I_q K_d)}{V_1(T(s)-1)} \tag{16}$$

where $I_d + jI_q = I_1\cos(\phi_{i1}) + jI_1\sin(\phi_{i1})$. It should be noted that I_d and I_q represent the values of *d*-axis and *q*-axis current, rather than the signal itself.

After adding these compensation terms, it is possible to successfully make the coefficient term of V_1 become 0. However, due to $T(s)/V_1(T(s)-1) = -H_{pll}(s)$, it will introduce an additional integral component $\frac{1}{s}$ to the entire compensation term. Under weak grid, there can be significant fluctuations in the *q*-axis voltage [19]. The integration term amplifies these fluctuations, which may have a negative impact on the stability of the system [16]. Therefore, this article adopts $V_1(T(s)+1)$ to replace $V_1(T(s)-1)$ in (15) and (16), thereby avoiding the occurrence of the aforementioned issues. Since this article focuses on the oscillation issues in the mid and high frequency range of GCI, $(T(s)-1)/(T(s)+1) \approx 1$, using $V_1(T(s)+1)$ achieves the same effect as compensating with $V_1(T(s)-1)$. Therefore, the new compensation terms are

$$G_d(s) = \frac{T(s)(I_d K_d - I_q H_i(s))}{V_1(T(s)+1)} \tag{17}$$

$$G_q(s) = -\frac{T(s)(I_d H_i(s) + I_q K_d)}{V_1(T(s)+1)}. \tag{18}$$

The current control loop with added compensation control is shown in Fig. 11. After incorporating compensation control, the expressions for the modulated waves c_a in the frequency domain can be obtained as

$$\mathbf{c}_a[f] = \begin{cases} (-H_i(s \mp j2\pi f_1) \pm jK_d)G_i(s)\mathbf{I}_p & f = \pm f_p \\ (-H_i(s \pm j2\pi f_1) \mp jK_d)G_i(s)\mathbf{I}_n & f = \pm f_n. \end{cases} \tag{19}$$

Then, the equivalent impedance model of the GCI after compensation control can be obtained

$$Z_{1np}(s) = \frac{sL_f + \frac{V_{dc}}{2}(H_i(s - j2\pi f_1) - jK_d)G_i(s)}{1 - \frac{V_{dc}}{2}K_f G_v(s)} \tag{20}$$

$$Z_{1nn}(s) = \frac{sL_f + \frac{V_{dc}}{2}(H_i(s + j2\pi f_1) + jK_d)G_i(s)}{1 - \frac{V_{dc}}{2}K_f G_v(s)}. \tag{21}$$

According to (20) and (21), it can be seen that the equivalent impedance of the GCI no longer contains V_1, and its equivalent impedance does not change with the change of V_1, which can effectively avoid the appearance of the instability region. It can make the stable operation of the GCI under weak grid and high PLL bandwidth.

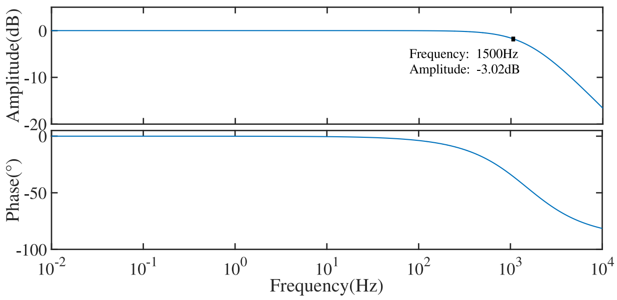

Fig. 12. Bode diagram of the current controller when the controller is designed as $28.2 + 12/s$.

B. Selection of Parameters for the Current Control Loop

In previous section, a compensation control method based on *q*-axis voltage, which decouples the GCI equivalent impedance from the PLL, voltage and current is proposed. Based on (20) and (21), it is clear that the equivalent impedance is only related to the current controller parameters. To ensure the system maintain good dynamic performance under weak grid conditions, this section will design parameters for current controller.

According to [16], the closed-loop transfer function of the current control loop is $G_c(s) = G_o(s)/(1 + G_o(s))$, in which $G_o(s) = (k_{pi} + k_{ii}/s)/sL_f$ is the open loop gain. In classical control theory, the bandwidth ω_{bw} of the closed-loop system is defined as the frequency at which the gain decreases by 3 dB from its gain at $\omega = 0$ [29]. The larger ω_{bw}, the better the dynamic performance of the system. Meanwhile, ω_{bw} should be less than 1/10 of the inverter switching frequency [30]. The switching frequency of the GCI used in this article is 20 kHz. To balance the system control performance with the design requirements, ω_{bw} of 1500 Hz are selected for the current loop. In summary, when the filter inductance L_f is selected as 3 mH, the current controller is designed as $28.2 + 12/s$, with a control bandwidth of 1500 Hz. As shown in Fig. 12, the Bode plot of the current controller crosses −3 dB at 1500 Hz. Therefore, the parameters of the current control loop meet the design requirements, ensuring good dynamic performance of the current control in the system. In the subsequent simulations and experiments, the control parameters obtained will be used.

V. SIMULATION RESULTS

In this section, the effectiveness of the stability analysis method proposed and the stability enhancement method proposed in this article are severally verified through MATLAB/Simulink. Thereinto, the system topology is depicted in Fig. 1. The system parameters are provided in Table I.

A. Effectiveness of the Stability Analysis Method Proposed

According to the analysis results in Section III, it is evident that when Z consistently resides within the stable region, the system is bound to be stable. Conversely, instability issues arise when the synthesized impedance falls outside this stable region. This article validates the proposed method by adjusting the line

TABLE II
TEST SITUATIONS

Situations	$R_g(\Omega)$	L_g(mH)	Output power(kW)	PLL bandwidth(Hz)
Situation 1	0.04	4	10	130
Situation 2	0.04	4	20	130
Situation 3	0.04	14	10	130
Situation 4	0.04	4	10	220

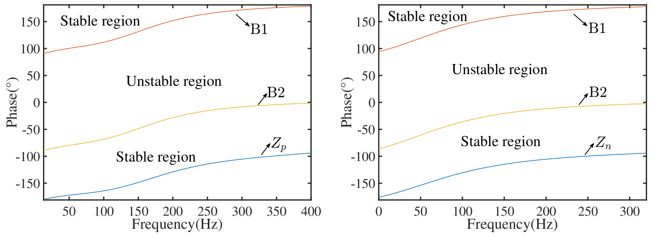

(a) (b)

Fig. 13. Schematic diagram of the region where $Z_{p(n)}$ is located under situation 1: R_g is 0.04 Ω, L_g is 4 mH, output power is 10 kW and PLL bandwidth is 130 Hz. (a) Positive sequence impedance, stable. (b) Negative sequence impedance, stable.

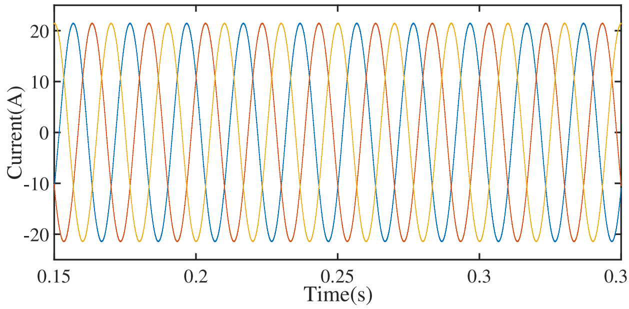

Fig. 14. Simulation result of the GCI output current under situation 1: R_g is 0.04 Ω, L_g is 4 mH, output power is 10 kW and PLL bandwidth is 130 Hz.

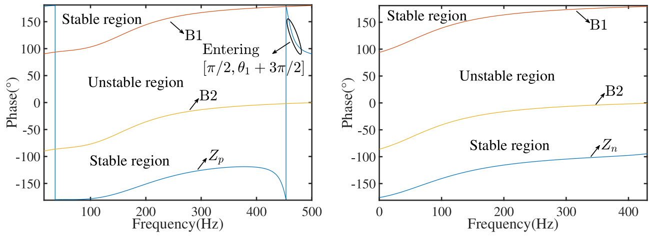

(a) (b)

Fig. 15. Schematic diagram of the region where $Z_{p(n)}$ is located under situation 2: R_g is 0.04 Ω, L_g is 4 mH, output power is 20 kW and PLL bandwidth is 130 Hz. (a) Positive sequence impedance, unstable. (b) Negative sequence impedance, stable.

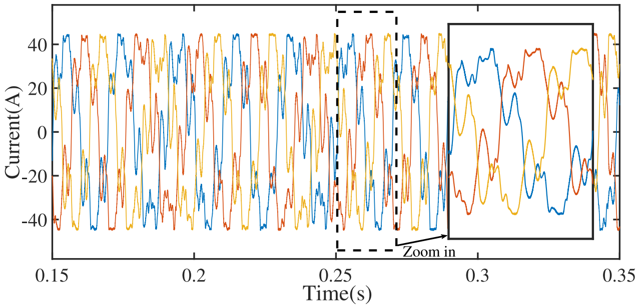

Fig. 16. Simulation result of the GCI output current under situation 2: R_g is 0.04 Ω, L_g is 4 mH, output power is 20 kW and PLL bandwidth is 130 Hz.

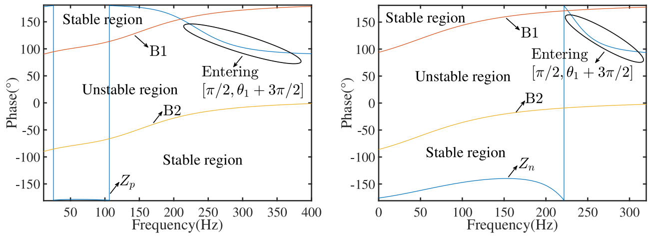

(a) (b)

Fig. 17. Schematic diagram of the region where $Z_{p(n)}$ is located under situation 3: R_g is 0.04 Ω, L_g is 14 mH, output power is 10 kW and PLL bandwidth is 130 Hz. (a) Positive sequence impedance, unstable. (b) Negative sequence impedance, unstable.

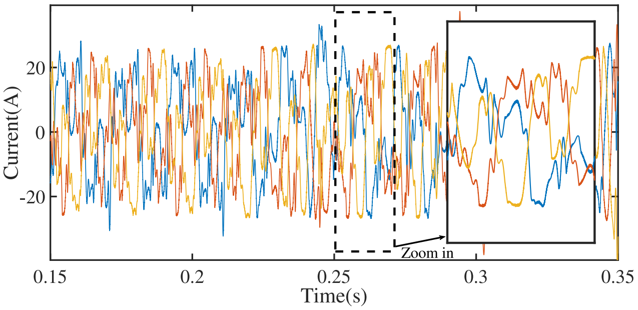

Fig. 18. Simulation result of the GCI output current under situation 3: R_g is 0.04 Ω, L_g is 14 mH, output power is 10 kW and PLL bandwidth is 130 Hz.

impedance, the output power of the GCI and the PLL bandwidth to position the synthesized impedance within different regions. The effectiveness of the analysis method is then verified based on the output current of the GCI. The test situations are shown in Table II.

In order to make the simulation verification results more intuitive, this article defines the boundary of the positive half axis of the y-axis in Fig. 9 as B1 and the boundary of the negative half axis of the y-axis as B2. The simulation results of the four testing situations are shown in Figs. 13, 15, 17, and 19. The vertical axis range of the simulation results is $[-180°, 180°]$, corresponding to Fig. 9. The horizontal axis represents the frequency band where the GCI output impedance is negative impedance. The simulation diagram contains three curves, namely B1, B2, and the system synthesis impedance Z_p (or Z_n). The region between B1 and B2 is the unstable region, while the remaining region is the stable region. When Z_p (or Z_n) passes through the unstable region, it represents system instability. On the contrary, the system remains stable.

For situation 1, the region in which the synthesized impedance phase θ of the grid-connected system is located as shown in Fig. 13. The positive sequence phase and negative sequence phase is always in the stable range, indicating that the system is

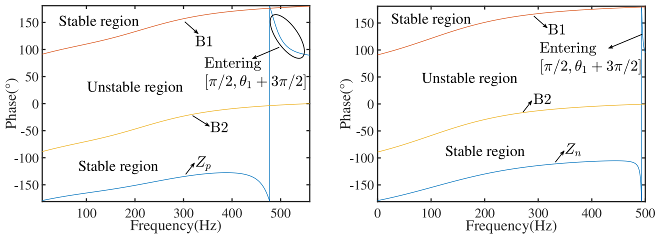

(a) (b)

Fig. 19. Schematic diagram of the region where $Z_{p(n)}$ is located under situation 4: R_g is 0.04 Ω, L_g is 4 mH, output power is 10 kW and PLL bandwidth is 220 Hz. (a) Positive sequence impedance, unstable. (b) Negative sequence impedance, unstable.

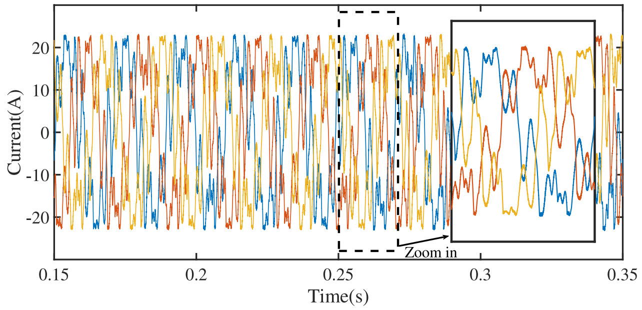

Fig. 20. Simulation result of the GCI output current under situation 4: R_g is 0.04 Ω, L_g is 4 mH, output power is 10 kW and PLL bandwidth is 220 Hz.

inherently stable. The output current of the GCI is illustrated in Fig. 14, confirming the stability of the system.

For situation 2, the region in which the synthesized impedance phase θ is located as shown in Fig. 15. Although the negative sequence impedance consistently remains within the stable region, the positive sequence impedance enters the unstable region $[\pi/2, \theta_1 + 3\pi/2]$ in the high frequency range. In this case, the system will experience instability. The output current of the GCI is depicted in Fig. 16, confirming the occurrence of instability in the system.

For situation 3, the region in which the synthesized impedance phase θ resides is shown in Fig. 17. Both positive and negative sequence phase enter the instability region $[\pi/2, \theta_1 + 3\pi/2]$ in the high frequency range. In this case, the system will experience instability. The output current of the GCI is illustrated in Fig. 18, confirming the occurrence of instability in the system.

For the situation 4, the region in which the synthesized impedance phase θ resides is shown in Fig. 19. Similar to the situation 3, both positive and negative sequence phase enter the instability region $[\pi/2, \theta_1 + 3\pi/2]$ in the high frequency range. In this case, the system will experience instability. The output current of the GCI is illustrated in Fig. 20, confirming the occurrence of instability in the system.

The above four sets of simulation results validate the effectiveness of the analysis method proposed. In addition, they confirm the explanatory mechanism in this article regarding the susceptibility of GCI to instability under weak grid and high PLL bandwidth.

TABLE III
TEST CASES

Cases	L_g(mH)	Output power(kW)	SCR	PLL bandwith(Hz)
Case 1	6	8	6.4	70
Case 2	12	13	2	130
Case 3	16	18	1	220

B. Performance Analysis of the Proposed Compensation Control Method

To validate the effectiveness and performance of the compensation control method proposed in this article, test data as shown in Table III are employed. Table III includes three cases, labeled from case 1 to case 3, where the GCI output power, line impedance, and PLL bandwidth gradually increase, indicating increasingly challenging operating conditions for the system. The relationship between PLL bandwidth and PI parameters can be found in [31]. The simulation results of GCI output current without additional control are shown in Fig. 21. At low output power, line impedance and PLL bandwidth, GCI operates stably. However, as the system operating conditions become more adverse, instability occurs in GCI. This greatly limits the application of GCI under weak grid. The simulation results of GCI output current based on the compensation control are shown in Fig. 22. In all cases, GCI remains stable. The proposed method in this article eliminates the coupling between GCI and voltage, enhancing the system stability without sacrificing dynamic performance.

Furthermore, in practical operation, GCI may work under nonunity power factor conditions [32]. However, most research commonly assumes the power factor of 1 for GCI and proposes corresponding stability enhancement methods, which is evidently unrealistic. According to (20) and (21), the solution presented in this article also eliminates the coupling between GCI and the q-axis current, ensuring system stability under nonpower factor condition. Therefore, in case 3, keeping other parameters constant and setting the q-axis current to 3 A, the simulation results are shown in Fig. 23. Fig. 23(a) shows the tracking performance of the d-axis and q-axis current of GCI, while Fig. 23(b) presents the waveform of GCI output current. The simulation results indicate that under nonpower factor condition, the system can still operate stably, and the d-axis and q-axis currents can track the set values effectively.

In summary, the comprehensive simulation analysis effectively validates the performance of the proposed method under weak grid and high PLL bandwidth, as well as under non-unity power factor situation.

C. Comparison With State-of-the-art Methods

This article reveals that the emergence of instability regions is caused by the impedance varying with voltage changes. Accordingly, a q-axis voltage compensation method is proposed to decouple impedance from voltage and avoid the occurrence of instability regions. However, existing methods cannot achieve complete decoupling of impedance and voltage, preventing them from the operational capability of GCI under weak grid and high

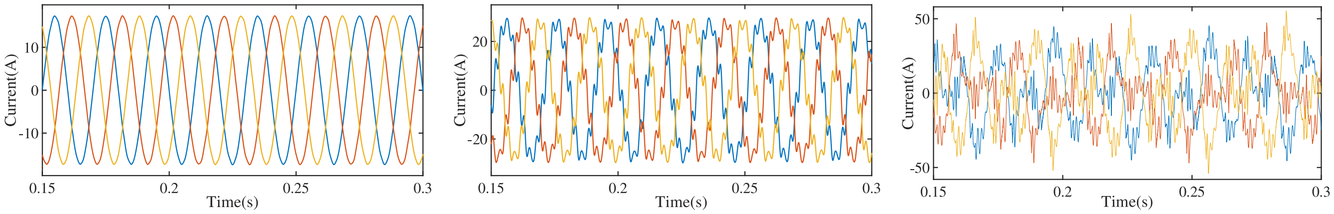

(a) (b) (c)

Fig. 21. Simulation results of the GCI output current without additional control under different cases. (a) Case 1: L_g is 6 mH, output power is 8 kW and PLL bandwidth is 70 Hz. (b) Case 2: L_g is 12 mH, output power is 13 kW and PLL bandwidth is 130 Hz. (c) Case 3: L_g is 16 mH, output power is 18 kW and PLL bandwidth is 220 Hz.

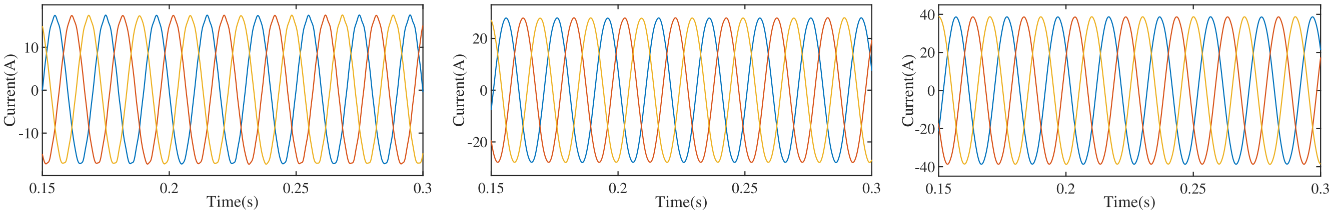

(a) (b) (c)

Fig. 22. Simulation results of the GCI output current with the method proposed under different cases. (a) Case 1: L_g is 6 mH, output power is 8 kW and PLL bandwidth is 70 Hz. (b) Case 2: L_g is 12 mH, output power is 13 kW and PLL bandwidth is 130 Hz. (c) Case 3: L_g is 16 mH, output power is 18 kW and PLL bandwidth is 220 Hz.

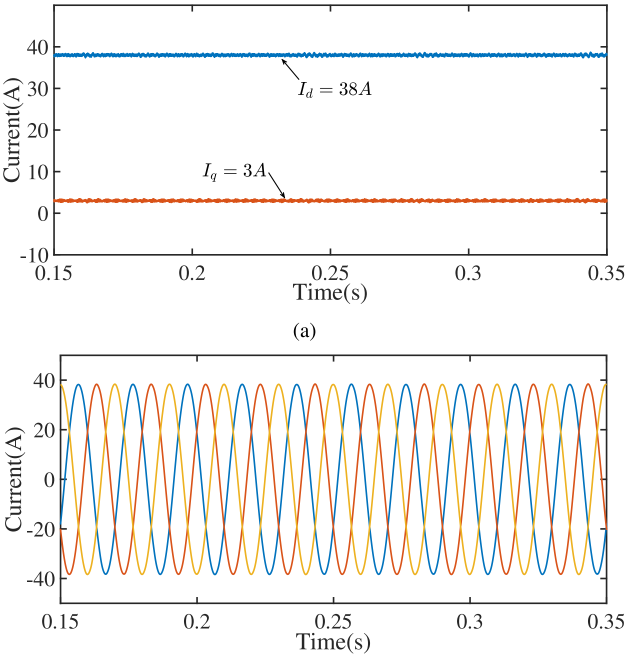

Fig. 23. Simulation results of the GCI output current with the method proposed under nonpower factor condition. (a) GCI output d-axis and q-axis current. (b) GCI output current.

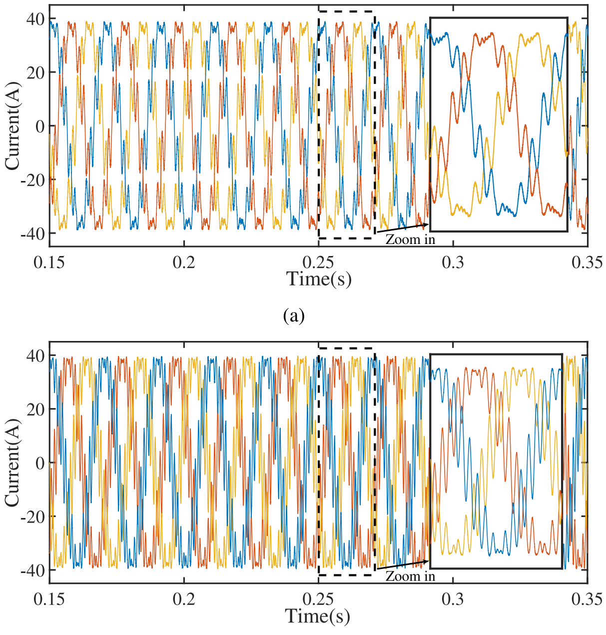

(b)

Fig. 24. Simulation results of the GCI output current with different methods under case 3: L_g is 16 mH, output power is 18 kW and PLL bandwidth is 220 Hz. (a) Method proposed in [16]. (b) Method proposed in [17].

PLL bandwidth. The design principles and drawbacks of existing methods are shown in Table IV.

The authors in [11] and [12] proposed improving system stability by reducing the PLL bandwidth. The authors in [13] and [14] provided guidelines for selecting the controller parameters for both the PLL and current controller. However, such methods often involve a complex parameter design process and are likely to reduce the dynamic response speed of the system. In addition, they cannot eliminate the coupling between impedance

TABLE IV
COMPARISON WITH STATE-OF-THE-ART METHODS

Method	Literature	Design approach	Drawbacks
PLL parameter design	[11], [12]	Reduce the PLL bandwidth.	The parameter design process is complex; affect the dynamic response speed; impedance and voltage cannot be decoupled.
	[13], [14]	Select the controller parameters for both the PLL and current controller.	
Decoupling PLL and impedance	[15]	Decouple between the PLL and grid impedance.	Rely on the accurate online grid impedance measurement.
	[16]	A constant coupling effect-based PLL is proposed.	Changes in voltage and current can affect the coupling.
Symmetrical PLL structure	[33]	Introduce a complex phase angle to capture the grid voltage dynamics on both the q-axis and d-axis.	Impedance and voltage cannot be decoupled; the design process is complex.
Phase compensation in PLL	[34]	Compensate PLL angle based on estimated or measured grid impedance.	Rely on the accurate online grid impedance measurement; the compensation term is related to the grid impedance.
	[35]	Select the artificial bus between the PCC and the grid as the reference for PLL.	
State feedback controller	[36]	Add full state feedback to the current loop to increase the damping.	The design process is complex and it is difficult to implement.
	[37]	Combine robust $H-\infty$ optimal control with full state feedback.	
Impedance reshaping / Virtual impedance	[38]	Reshape the q-axis impedance of GCI into a positive resistance.	Ignore the coupling between the voltage and d-axis.
	[39]	Compensate the GCI impedance phase at the frequency of the intersection.	Rely on the accurate online grid impedance measurement.
	[40]	Configure virtual impedance loop to adjust GCI output impedance.	Impedance and voltage cannot be decouple; poor robustness.
Current loop compensation control	[17]	Introduce q-axis voltage compensation in q-axis.	Ignore the coupling between the voltage and d-axis.
	[18]	Introduce d-axis voltage compensation in the d-axis and introduce q-axis voltage compensation in q-axis.	d-axis and voltage cannot be decoupled.
	[19]	Introduce q-axis voltage compensation separately in d-axis and q-axis.	Ignore the coupling introduced by the current decoupling term with the voltage.
	[41]	Add V_α and V_β compensation in the stationary frame.	Not applicable to GCI with PLL; impedance and voltage cannot be decoupled.
	Proposed	Introduce q-axis voltage compensation separately in d-axis and q-axis; Realize complete decoupling between GCI impedance and voltage to avoid the occurrence of unstable regions.	

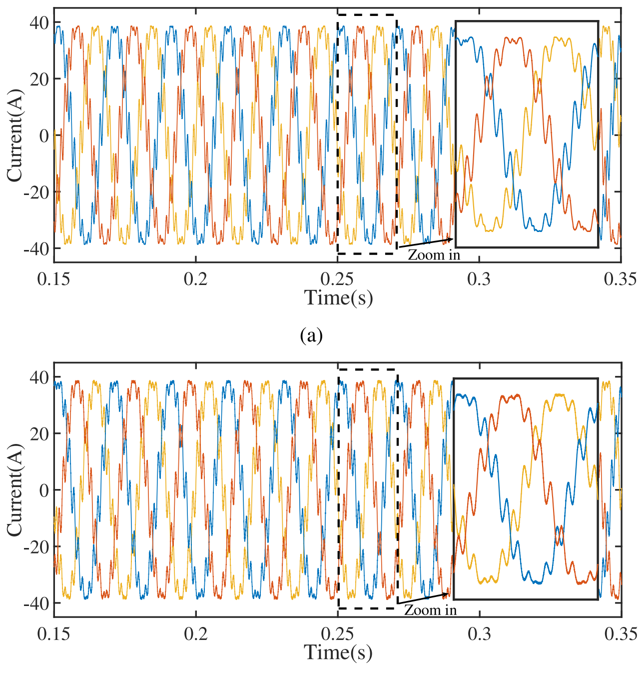

(a)

(b)

Fig. 25. Simulation results of the GCI output current with different methods under case 3: L_g is 16 mH, output power is 18 kW and PLL bandwidth is 220 Hz. (a) Method proposed in [19]. (b) Method proposed in [38].

and voltage. The authors in [15] proposed a decoupling strategy between the PLL and grid impedance, making the PLL bandwidth independent of system stability. However, this method relies on accurate online grid impedance measurements, which reduces its reliability. The authors in [16] introduced a PLL based on a constant coupling effect, but the coupling term depends on the output voltage, and voltage variations affect the degree of coupling. Moreover, the design process for these methods is also complex. Furthermore, [33] proposed a symmetrical PLL structure. This method introduces a complex phase angle to capture the grid voltage dynamics on both the q-axis and d-axis. However, it is difficult to achieve decoupling between the GCI impedance and voltage. The authors in [34] and [35] proposed compensating the PLL using estimated grid impedance values or an artificial bus between the PCC and the grid. However, such methods also rely on online grid impedance measurements. The authors in [36] and [37] designed state feedback controllers to enhance the stability of GCI, but the design process of such methods is very complex and difficult to implement.

Compared with modifying the PLL structure and feedback controller design, impedance reshaping/virtual impedance methods and current loop compensation control methods also have been widely applied. The authors in [38] reshaped the q-axis impedance of GCI into a positive resistance, but this method ignores the coupling between the voltage and d-axis. The authors in [39] proposed an impedance adjustment scheme to

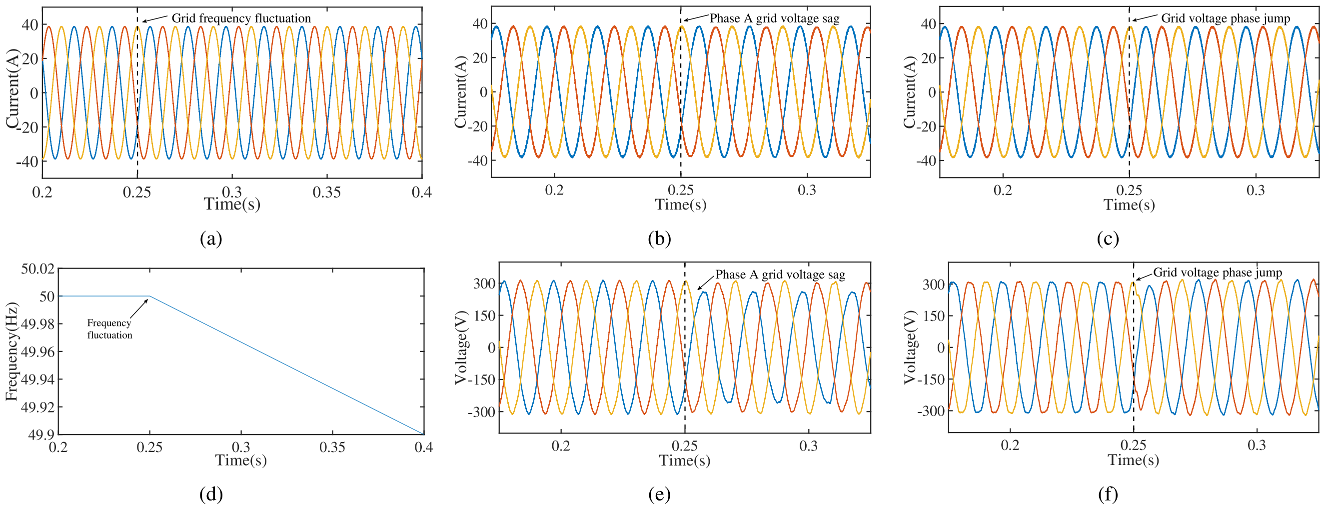

Fig. 26. Simulation results of the GCI output current, frequency and voltage with the method proposed under different disturbances in case 3: L_g is 16 mH, output power is 18 kW and PLL bandwidth is 220 Hz. (a) GCI output current under grid voltage frequency fluctuation. (b) GCI output current under phase A grid voltage sag. (c) GCI output current under grid voltage phase jump. (d) Grid voltage frequency fluctuation of 0.1 Hz. (e) Phase A grid voltage sag by 12%. (f) Grid voltage phase jump of $\pi/10$ (18°).

ensure that when the impedance magnitudes intersect, the phase difference is less than 180°, but this method relies on accurate measurement of grid impedance. The authors in [40] configured virtual impedance loop to adjust the GCI output impedance. However, this method cannot achieve complete decoupling of impedance and voltage, and it has poor robustness. The compensation method in [17] only acts on the *q*-axis, ignoring the voltage coupling introduced by the *d*-axis. Meanwhile, the method proposed in [17] introduces an integral term $1/s$ in the compensation term, which can have adverse effects in weak grid. The method in [18] introduced *d*-axis voltage compensation on the *d*-axis and *q*-axis voltage compensation on the *q*-axis, respectively. However, the V_1 term introduced by the *d*-axis is mainly related to the *q*-axis voltage. The PLL tracks phase based on the *q*-axis voltage. Therefore, this method also cannot achieve complete decoupling between the *d*-axis and voltage. Meanwhile, this method focuses more on eliminating the coupling introduced by the dc outer loop. When the influence of the dc outer loop is not considered, this method is similar to the method proposed by [17]. The method in [19] ignores the voltage coupling introduced by the current decoupling term. The authors in [41] proposed introducing V_α and V_β compensation in the stationary reference frame, but this method is not suitable for GCI with PLL. In conclusion, compared with the present control methods, the method proposed can more easily and significantly enhance GCI operational capability in weak grid and exhibit stronger robustness.

In this section, we will compare the methods proposed in [16], [17], [19], and [38] with the method proposed in this article under case 3. The simulation results of the methods proposed in [16], [17], [19], and [38] are shown in Figs. 24 and 25. The simulation results indicate that the output currents of all four stability enhancement methods generate significant oscillations, making it challenging to ensure the stable operation of the system. In comparison to Fig. 22(c), the method proposed in this article clearly outperforms the stability enhancement solutions suggested in the aforementioned references.

D. Performance Analysis Under System Disturbances

In practical scenarios, system disturbances are inevitable, such as fluctuations in grid voltage frequency, grid voltage drops, and phase jumps in grid voltage [16]. The simulated waveforms of the GCI based on compensation control are illustrated in Fig. 26. Among them, Fig. 26(a)–(c) represent the corresponding current waveforms during fluctuations in grid voltage frequency, sudden drops in grid voltage and phase jumps in grid voltage, respectively. Fig. 26(d) shows the result when the grid voltage frequency gradually decreases from the nominal value. Fig. 26(e) depicts the result when the phase A grid voltage drops by 12% from the nominal value while the other phases remain at the nominal value. Fig. 26(f) presents the result when there is a phase jump of $\pi/10$ (18°) in the three-phase grid voltage.

It can be observed that the system remains stable under various disturbances. The compensation control method designed enables the system to accurately estimate the grid phase even in scenarios with high PLL bandwidth, facilitating precise control. Simulation results indicate that this method exhibits excellent disturbance rejection capabilities and can enhance the transient performance of the system under disturbances. The above four sets of simulation results align well with theoretical analysis. Therefore, the proposed compensation control method can be considered as an effective solution for enhancing the stability of GCI.

VI. EXPERIMENTAL RESULTS

In this section, an experimental test is conducted to verify the effectiveness of the stability analysis method proposed and the stability enhancement scheme based on compensation. The controller hardware-in-the-loop (CHIL) experiments are

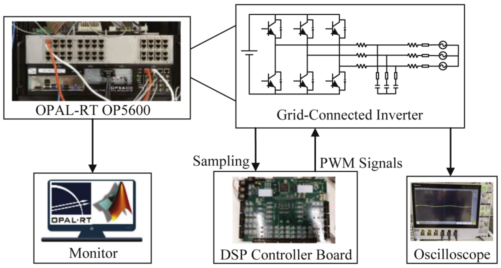

Fig. 27. CHIL experiment topology.

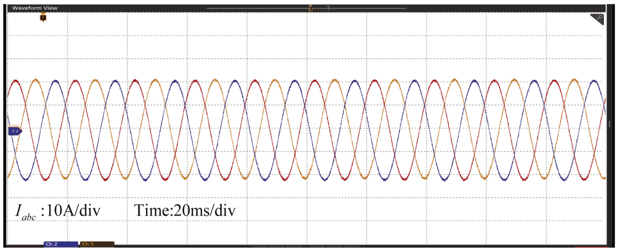

Fig. 28. Experimental result of the GCI output current under situation 1: R_g is 0.04 Ω, L_g is 4 mH, output power is 10 kW and PLL bandwidth is 130 Hz.

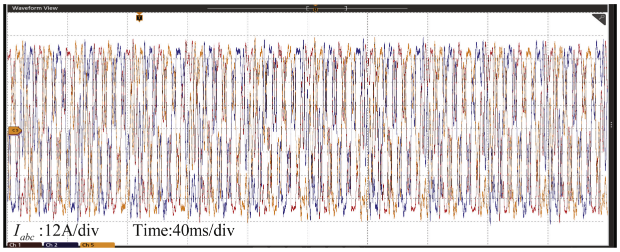

Fig. 29. Experimental result of the GCI output current under situation 2: R_g is 0.04 Ω, L_g is 4 mH, output power is 20 kW and PLL bandwidth is 130 Hz.

set in OPAL-RT real-time simulator. In this CHIL experiment, the traditional control strategy and compensation-based control method for GCI are embedded into one DSP(TMS320F28335) controller when the other elements are simulated through the OPAL-RT real-time simulator, which are seen in Fig. 27. Meanwhile, the detailed section can be found in [42]. The parameters of the relevant experimental test system are the same as those of the simulation system in Table I.

A. *Effectiveness of the Stability Analysis Method Proposed*

In this section, experimental validation will be conducted for the situations listed in Table II. The experimental results are shown in Figs. 28–31. The results indicate that GCI is only stable in the situation 1, while in the other three situations, the output waveform exhibits significant oscillations, and the GCI cannot operate stably. According to the analysis results in Figs. 13, 15, 17, and 19, the synthetic impedance Z remains within the stability region only in the situation 1; in the other situations, Z enters the instability region. Therefore, GCI can operate stably only in the situation 1. The experimental results are consistent with the theoretical analysis, which validates the correctness of the proposed stability discrimination regions.

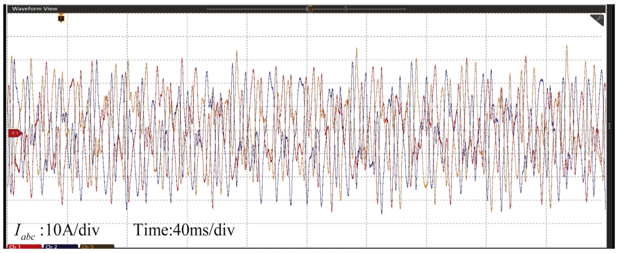

Fig. 30. Experimental result of the GCI output current under situation 3: R_g is 0.04 Ω, L_g is 14 mH, output power is 10 kW and PLL bandwidth is 130 Hz.

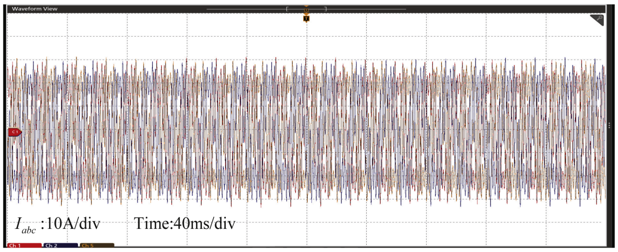

Fig. 31. Experimental result of the GCI output current under situation 4: R_g is 0.04 Ω, L_g is 4 mH, output power is 10 kW and PLL bandwidth is 220 Hz.

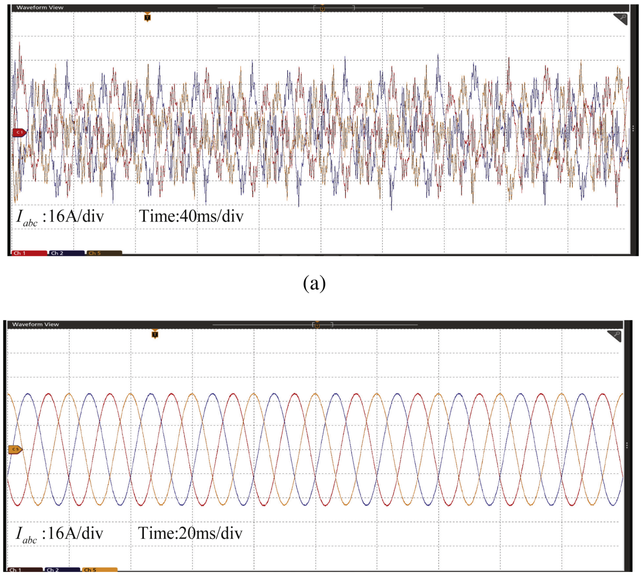

(a)

(b)

Fig. 32. Experimental results of the GCI output current with different methods under case 3: L_g is 16 mH, output power is 18 kW and PLL bandwidth is 220 Hz. (a) Without additional control. (b) Method proposed in this article.

B. *Effectiveness of the Stability Enhancement Method Proposed*

In this section, experimental validation will be conducted using the parameters from case 3 in Table III. The experimental result without control is shown in Fig. 32(a). The experimental

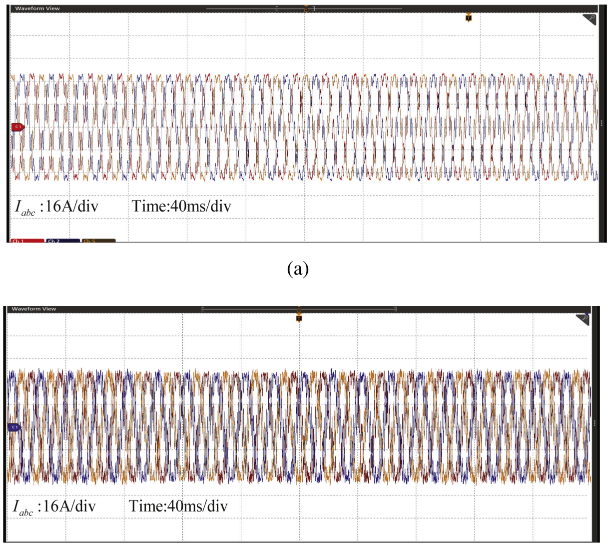

(a)

(b)

Fig. 33. Experimental results of the GCI output current with different methods under case 3: L_g is 16 mH, output power is 18 kW and PLL bandwidth is 220 Hz. (a) Method proposed in [16]. (b) Method proposed in [17].

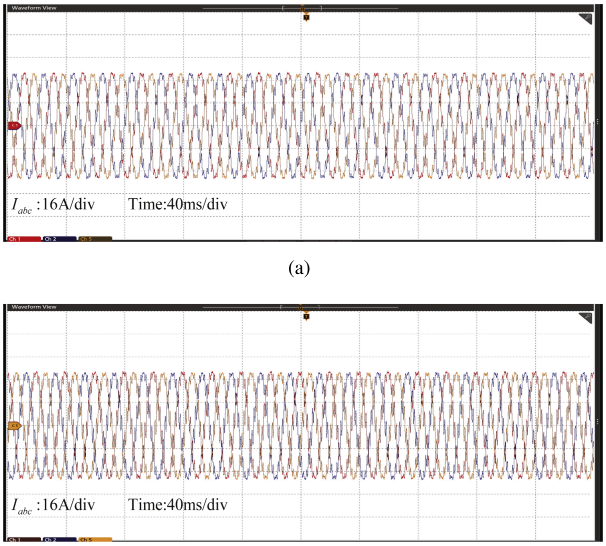

(a)

(b)

Fig. 34. Experimental results of the GCI output current with different methods under case 3: L_g is 16 mH, output power is 18 kW and PLL bandwidth is 220 Hz. (a) Method proposed in [19]. (b) Method proposed in [38].

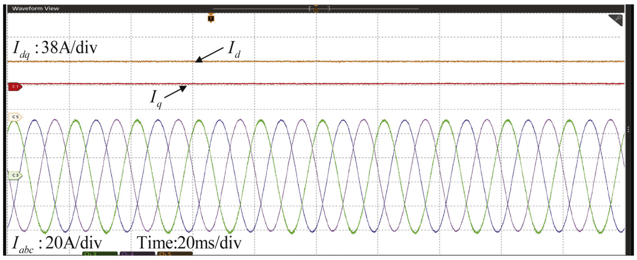

Fig. 35. Experimental results of the GCI output current with the method proposed under nonpower factor condition.

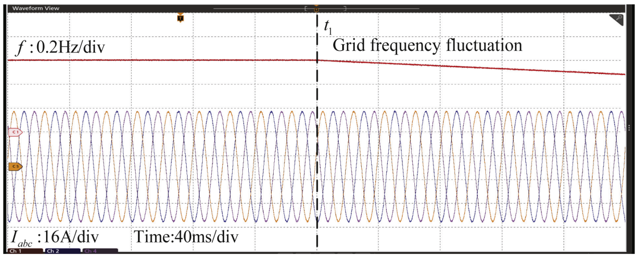

Fig. 36. Experimental results of the GCI output current and frequency with the method proposed under grid voltage frequency fluctuation of 0.1 Hz in case 3: L_g is 16 mH, output power is 18 kW and PLL bandwidth is 220 Hz.

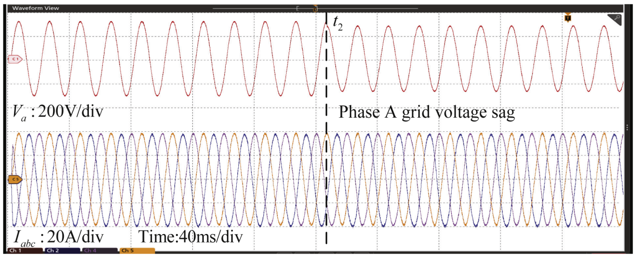

Fig. 37. Experimental results of the GCI output current and voltage with the method proposed under phase A grid voltage sag by 12% in case 3: L_g is 16 mH, output power is 18 kW and PLL bandwidth is 220 Hz.

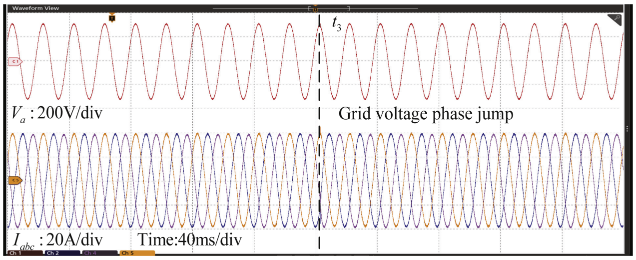

Fig. 38. Experimental results of the GCI output current and voltage with the method proposed under grid voltage phase jump of $\pi/10$ (18°) in case 3: L_g is 16 mH, output power is 18 kW and PLL bandwidth is 220 Hz.

result of the proposed method is shown in Fig. 32(b). The results of the control methods proposed in [16], [17], [19] and [38] are shown in Figs. 33 and 34. Through comparison, it is found that only the method proposed in this article enables GCI to operate stably under extremely weak grid and high PLL bandwidth. Under the other control methods, the output waveform of the GCI exhibits significant distortion, and GCI becomes unstable. This further validates the effectiveness of the proposed method.

Fig. 35 shows the operating conditions of GCI under nonpower factor conditions after applying the proposed method, using the parameters from case 3 in Table III. The experimental results indicate that GCI can still operate stably.

Figs. 36–38 illustrate the operating performance of GCI under system disturbances after applying the proposed method. At t_1, t_2, and t_3, GCI experiences fluctuations in grid voltage frequency, sudden drops in grid voltage, and phase jumps in grid voltage, respectively. The specific disturbances correspond to the values used in the simulation experiments. The experimental results demonstrate that GCI can still achieve precise current control, ensuring stable operation of the system.

The conclusions drawn from the hardware experiments are consistent with those from the simulation experiments. This further validates the effectiveness of the proposed method and its superiority over existing control strategies.

VII. CONCLUSION

This article has proposed a more general stability analysis method for GCI, providing a clear physical explanation for GCI instability and further obtaining the instability conditions when GCI exhibits negative impedance. The research results indicate that, GCI instability arises due to the interaction between the fundamental and nonfundamental voltage at the PCC. This interaction will exacerbate the oscillation of system voltage, leading to instability issues. Furthermore, a new impedance-based stablility discrimination region has been obtained. Under weak grid conditions and high PLL bandwidth, the system equivalent impedance is prone to entering the unstable region. The generation of the instability region is attributed to the variation in the equivalent impedance of GCI with changing PCC voltage.

Furthermore, to enhance GCI stability under weak grid conditions and high PLL bandwidth, a simple *q*-axis voltage compensation control method has been proposed. This method decouples the GCI output impedance from the voltage, thus avoiding the emergence of instability regions. It significantly improves GCI operational capability under adverse conditions, endowing GCI with robust disturbance resistance and transient performance during system perturbations.

APPENDIX A
SEQUENCE IMPEDANCE MODELING OF THE GCI

In the time domain, after adding small-signal perturbations, the phase A output terminal voltage and output current of the GCI are as follows:

$$\begin{aligned} v_a(t) &= V_1\cos(2\pi f_1 t) + V_p\cos(2\pi f_p t + \phi_{vp}) \\ &\quad + V_n\cos(2\pi f_n t + \phi_{vn}) \end{aligned} \tag{A.1}$$

$$\begin{aligned} i_a(t) &= I_1\cos(2\pi f_1 t + \phi_{i1}) + I_p\cos(2\pi f_p t + \phi_{ip}) \\ &\quad + I_n\cos(2\pi f_n t + \phi_{in}) \end{aligned} \tag{A.2}$$

where V_p and V_n are the amplitudes of the positive sequence voltage perturbation and negative sequence voltage perturbation, respectively; I_1, I_p, and I_n are the amplitudes of the fundamental current, positive sequence current perturbation, and negative sequence current perturbation, respectively; f_1, f_p, and f_n are the fundamental frequency, positive sequence perturbation frequency and negative sequence perturbation frequency, respectively; ϕ_{vp} and ϕ_{vn} are the initial phase angles of the positive sequence voltage perturbation and the negative sequence voltage perturbation, respectively; ϕ_{i1}, ϕ_{ip}, and ϕ_{in} are the initial phase angles of the fundamental current, positive sequence current response, and negative sequence current response, respectively.

From (A.1) and (A.2), the frequency-domain expressions of v_a and i_a can be described as follows:

$$\mathbf{V}_a[f] = \begin{cases} \mathbf{V_1}, & f = \pm f_1 \\ \mathbf{V}_p, & f = \pm f_p \\ \mathbf{V}_n, & f = \pm f_n \end{cases}, \mathbf{I}_a[f] = \begin{cases} \mathbf{I_1}, & f = \pm f_1 \\ \mathbf{I}_p, & f = \pm f_p \\ \mathbf{I}_n, & f = \pm f_n \end{cases} \tag{A.3}$$

where $\mathbf{V}_1 = V_1/2$; $\mathbf{V}_p = (V_p/2)e^{\pm j\phi_{vp}}$; $\mathbf{V}_n = (V_n/2)e^{\pm j\phi_{vn}}$; $\mathbf{I}_1 = (I_1/2)e^{\pm j\phi_{i1}}$; $\mathbf{I}_p = (I_p/2)e^{\pm j\phi_{ip}}$; $\mathbf{I}_n = (I_n/2)e^{\pm j\phi_{in}}$. The bold capital letters in the formula represent the frequency domain representation of the signal, including the amplitude, frequency, and phase information of the signal.

According to (3), assumed that the transfer function between the voltage perturbation and $\Delta\theta$ in the frequency domain is

$$\boldsymbol{\Delta\theta}[f] = \begin{cases} G_p(s)G_v(s \pm j2\pi f_1)\mathbf{V}_p, & f = \pm(f_p - f_1) \\ G_n(s)G_v(s \mp j2\pi f_1)\mathbf{V}_n, & f = \pm(f_n + f_1) \end{cases} \tag{A.4}$$

where $G_v(s)$ is the voltage sampling function, $G_v(s) = e^{-Ts}(1 - e^{-Ts})/[(Ts)(1 + s/\omega_v)]$ simulates the sampling delay, PWM delay and sampling low-pass filter. T is the sampling period, ω_v is the cutoff angle frequency of the low-pass filter.

According to (3) and (A.4), the expressions of v_d and v_q in the frequency domain can be obtained as

$$\mathbf{V}_d[f] = \begin{cases} V_1, & dc \\ G_v(s \pm j2\pi f_1)\mathbf{V}_p, & f = \pm(f_p - f_1) \\ G_v(s \mp j2\pi f_1)\mathbf{V}_n, & f = \pm(f_n + f_1) \end{cases} \tag{A.5}$$

$$\mathbf{V}_q[f] = \begin{cases} 0, & dc \\ (-G_p(s)V_1 \mp j) & \\ G_v(s \pm j2\pi f_1)\mathbf{V}_p, & f = \pm(f_p - f_1) \\ (-G_n(s)V_1 \pm j) & \\ G_v(s \mp j2\pi f_1)\mathbf{V}_n, & f = \pm(f_n + f_1). \end{cases} \tag{A.6}$$

Associating (A.4)–(A.6), the transfer function between the voltage perturbation and $\Delta\theta$ can be solved as

$$G_p(s) = \mp jH_{PLL}(s)/[1 + V_1 H_{PLL}(s)] \tag{A.7}$$

$$G_n(s) = \pm jH_{PLL}(s)/[1 + V_1 H_{PLL}(s)]. \tag{A.8}$$

Combining (A.3), (A.4), (A.7), and (A.8), the expressions for i_d and i_q in the frequency domain can be obtained as

$$\mathbf{I}_d[f] = \begin{cases} I_1\cos\phi_{i1}, & dc \\ \mp j\frac{T(s)}{V_1}G_v(s \pm j2\pi f_1)I_1 & \\ \sin\phi_{i1}\mathbf{V}_p + G_i(s \pm j2\pi f_1)\mathbf{I}_p, & f = \pm(f_p - f_1) \\ \pm j\frac{T(s)}{V_1}G_v(s \pm j2\pi f_1)I_1 & \\ \sin\phi_{i1}\mathbf{V}_n + G_i(s \pm j2\pi f_1)\mathbf{I}_n, & f = \pm(f_n + f_1) \end{cases} \tag{A.9}$$

$$\mathbf{I}_q[f]=\begin{cases} I_1\sin\phi_{i1}, & dc\\ \pm j\frac{T(s)}{V_1}G_v(s\mp j2\pi f_1)I_1 & \\ \cos\phi_{i1}\mathbf{V}_p\mp jG_i(s\mp j2\pi f_1)\mathbf{I}_p, & f=\pm(f_p-f_1)\\ \mp j\frac{T(s)}{V_1}G_v(s\mp j2\pi f_1)I_1 & \\ \cos\phi_{i1}\mathbf{V}_n\pm jG_i(s\mp j2\pi f_1)\mathbf{I}_n, & f=\pm(f_n+f_1)\end{cases}\tag{A.10}$$

where $T(s)=V_1H_{PLL}(s)/[1+V_1H_{PLL}(s)]$; $G_i(s)$ is the current sampling function, $G_i(s)=e^{-Ts}(1-e^{-Ts})/[(Ts)(1+s/\omega_i)]$ simulates the sampling delay, PWM delay, and sampling low-pass filter. ω_i is the cutoff angle frequency of the low-pass filter.

Associating (1), (2), (A.9), and (A.10), and based on the inverse dq coordinate transformation, the expressions for the modulated waves c_a in the frequency domain can be obtained as

$$\mathbf{c}_a[f]=\begin{cases} \mp j\frac{T(s\mp j2\pi f_1)}{2V_1}(H_i(s\mp j2\pi f_1)\mp jK_d) & \\ (-I_1\sin\phi_{i1}\pm jI_1\cos\phi_{i1})G_v(s)\mathbf{V}_p & \\ +[-H_i(s\mp j2\pi f_1)\pm jK_d]G_i(s)\mathbf{I}_p, & f=\pm f_p\\ \pm j\frac{T(s\pm j2\pi f_1)}{2V_1}(H_i(s\pm j2\pi f_1)\pm jK_d) & \\ (-I_1\sin\phi_{i1}\mp jI_1\cos\phi_{i1})G_v(s)\mathbf{V}_n & \\ +[-H_i(s\pm j2\pi f_1)\mp jK_d]G_i(s)\mathbf{I}_n, & f=\pm f_n.\end{cases}\tag{A.11}$$

According to Fig. 1(b), the frequency domain expression of m_a can be obtained as

$$\mathbf{m}_a[f]=\begin{cases} \mp j\frac{T(s\mp j2\pi f_1)}{2V_1}(H_i(s\mp j2\pi f_1) & \\ \mp jK_d)(-I_1\sin\phi_{i1}\pm jI_1\cos\phi_{i1}) & \\ G_v(s)\mathbf{V}_p+K_fG_v(s)\mathbf{V}_p+[-H_i(s & \\ \mp j2\pi f_1)\pm jK_d]G_i(s)\mathbf{I}_p, & f=\pm f_p\\ \pm j\frac{T(s\pm j2\pi f_1)}{2V_1}(H_i(s\pm j2\pi f_1) & \\ \pm jK_d)(-I_1\sin\phi_{i1}\mp jI_1\cos\phi_{i1}) & \\ G_v(s)\mathbf{V}_n+K_fG_v(s)\mathbf{V}_n+[-H_i(s & \\ \pm j2\pi f_1)\mp jK_d]G_i(s)\mathbf{I}_n, & f=\pm f_n.\end{cases}\tag{A.12}$$

The relationship between the inductance current, bridge arm midpoint voltage, and PCC voltage of the grid connected inverter can be obtained from Fig. 1(a) as follows:

$$sL_fi_a=\frac{V_{dc}}{2}m_a-v_a.\tag{A.13}$$

Substituting (A.3) and (A.12) into (A.13), the expressions for the positive and negative sequence impedance of GCI can be obtained as shown in (4) and (5) on Page 3, respectively.

Based on the above modeling process, it can be observed that I_1 is introduced when the current signal undergoes dq transformation via the PLL as shown in (A.9) and (A.10). Subsequently, it becomes coupled with the GCI output impedance through the current controller (and the current decoupling term) in (1)–(2) and line transmission relationship in (A.13). V_1 is introduced due to the phase-locked control of PLL. Subsequently, it follows the same transmission path as I_1 and is introduced into the GCI output impedance.

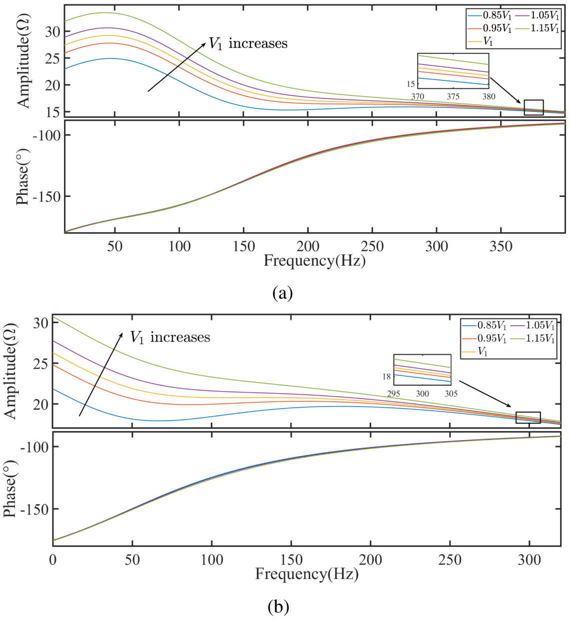

Fig. 39. GCI output impedance variation with V_1 when the PLL controller is set to $3.71+2145/s$ and the current controller is set to $28.2+12/s$. (a) Positive sequence impedance. (b) Negative sequence impedance.

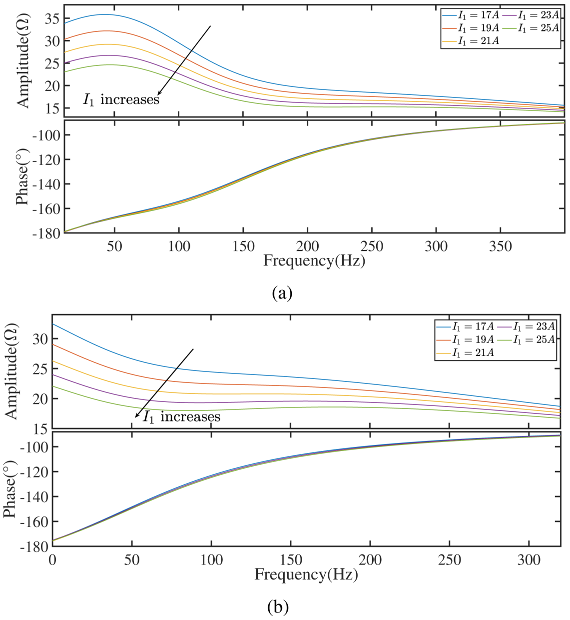

Fig. 40. GCI output impedance variation with I_1 when the PLL controller is set to $3.71+2145/s$ and the current controller is set to $28.2+12/s$. (a) Positive sequence impedance. (b) Negative sequence impedance.

APPENDIX B
SIMULATION VERIFICATION OF IMPEDANCE VARIATION WITH VOLTAGE AND CURRENT

To verify the universality of the conclusions drawn, this article conducts additional simulation validation of the GCI impedance model under different PLL parameters and current control loop

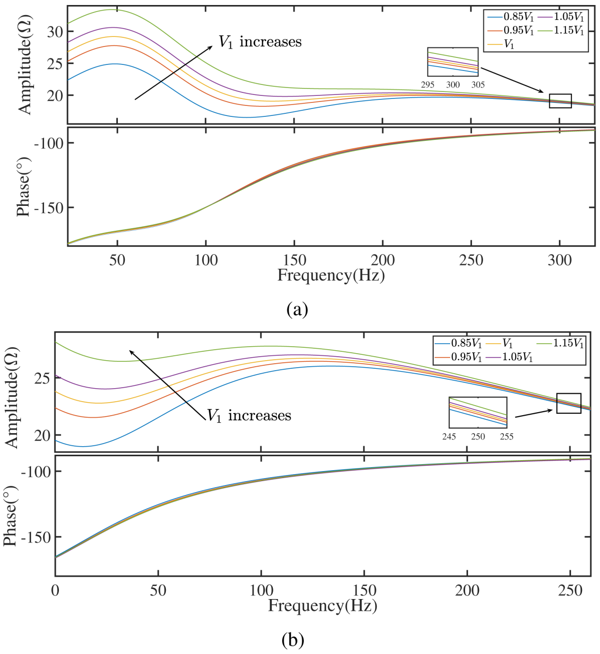

(a)

(b)

Fig. 41. GCI output impedance variation with V_1 when the PLL controller is set to $2.29 + 812.4/s$ and the current controller is set to $28.2 + 12/s$. (a) Positive sequence impedance. (b) Negative sequence impedance.

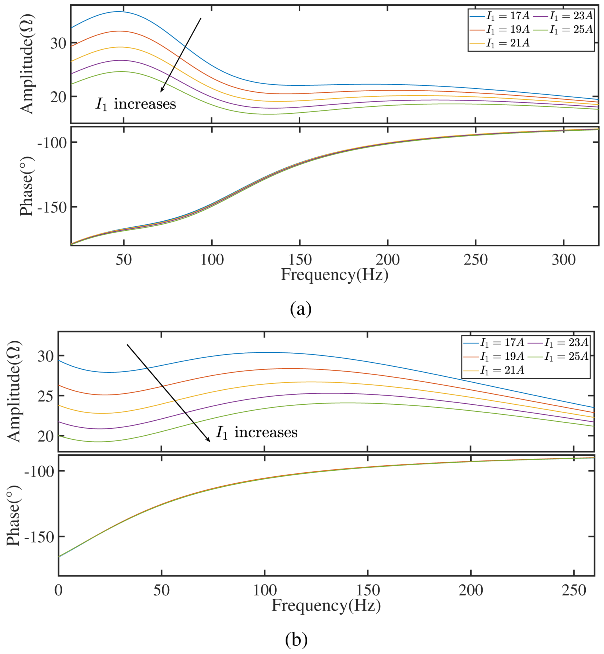

(a)

(b)

Fig. 42. GCI output impedance variation with I_1 when the PLL controller is set to $2.29 + 812.4/s$ and the current controller is set to $28.2 + 12/s$. (a) Positive sequence impedance. (b) Negative sequence impedance.

parameters. The simulation results are shown in Figs. 39–42. In Figs. 39 and 40, the PLL controller is set to $3.71 + 2145/s$ and the current controller is set to $28.2 + 12/s$. In Figs. 41 and 42, the PLL controller is set to $2.29 + 812.4/s$ and the current controller is set to $28.2 + 12/s$. It can be observed that under various control parameters, the impedance magnitude increases with the increase in voltage (or decrease in current), while the phase remains relatively unchanged. Therefore, the conclusion obtained of Section II-C is universal.

REFERENCES

[1] D. Li, Q. Sun, R. Wang, and Z. Sui, "Transient stability analysis and enhancement of inverter-based microgrid considering current limitation," *IEEE Trans. Power Electron.*, vol. 40, no. 1, pp. 2429–2441, Jan. 2025.

[2] A. Singhal, T. L. Vu, and W. Du, "Consensus control for coordinating grid-forming and grid-following inverters in microgrids," *IEEE Trans. Smart Grid*, vol. 13, no. 5, pp. 4123–4133, Sep. 2022.

[3] S. Zhou et al., "An improved design of current controller for LCL-type grid-connected converter to reduce negative effect of PLL in weak grid," *IEEE Trans. Emerg. Sel. Topics Power Electron.*, vol. 6, no. 2, pp. 648–663, Jun. 2018.

[4] D. Dong, B. Wen, D. Boroyevich, P. Mattavelli, and Y. Xue, "Analysis of phase-locked loop low-frequency stability in three-phase grid-connected power converters considering impedance interactions," *IEEE Trans. Ind. Electron.*, vol. 62, no. 1, pp. 310–321, Jan. 2015.

[5] D. Yang, X. Ruan, and H. Wu, "Impedance shaping of the grid-connected inverter with LCL filter to improve its adaptability to the weak grid condition," *IEEE Trans. Power Electron.*, vol. 29, no. 11, pp. 5795–5805, Nov. 2014.

[6] W. Rui, S. Qiuye, M. Dazhong, and H. Xuguang, "Line impedance cooperative stability region identification method for grid-tied inverters under weak grids," *IEEE Trans. Smart Grid*, vol. 11, no. 4, pp. 2856–2866, Jul. 2020.

[7] B. Wen, D. Boroyevich, R. Burgos, P. Mattavelli, and Z. Shen, "Analysis of D-Q small-signal impedance of grid-tied inverters," *IEEE Trans. Power Electron.*, vol. 31, no. 1, pp. 675–687, Jan. 2016.

[8] W. Wu et al., "Sequence-impedance-based stability comparison between VSGs and traditional grid-connected inverters," *IEEE Trans. Power Electron.*, vol. 34, no. 1, pp. 46–52, Jan. 2019.

[9] L. Hong, R. Tang, Q. Jiang, X. Xie, and Y. Zhu, "Admittance-based stability analysis of LCL-type grid-connected inverter considering AC-side and AC-DC frequency coupling effects," *IEEE Trans. Power Del.*, vol. 39, no. 3, pp. 1351–1363, Jun. 2024.

[10] F. Ma, H. Xin, D. Wu, Y. Liu, and X. Chen, "Assessing small-signal grid strength of 100% inverter-based power systems," *IEEE Trans. Power Del.*, vol. 39, no. 5, pp. 2784–2796, Oct. 2024.

[11] L. Harnefors, M. Bongiorno, and S. Lundberg, "Input-admittance calculation and shaping for controlled voltage-source converters," *IEEE Trans. Ind. Electron.*, vol. 54, no. 6, pp. 3323–3334, Dec. 2007.

[12] B. Wen, D. Dong, D. Boroyevich, R. Burgos, P. Mattavelli, and Z. Shen, "Impedance-based analysis of grid-synchronization stability for three-phase paralleled converters," *IEEE Trans. Power Electron.*, vol. 31, no. 1, pp. 26–38, Jan. 2016.

[13] D. Zhu, S. Zhou, X. Zou, and Y. Kang, "Improved design of PLL controller for LCL-type grid-connected converter in weak grid," *IEEE Trans. Power Electron.*, vol. 35, no. 5, pp. 4715–4727, May 2020.

[14] S. Golestan, M. Monfared, and F. D. Freijedo, "Design-oriented study of advanced synchronous reference frame phase-locked loops," *IEEE Trans. Power Electron.*, vol. 28, no. 2, pp. 765–778, Feb. 2013.

[15] X. Lin, J. Yu, R. Yu, J. Zhang, Z. Yan, and H. Wen, "Improving small-signal stability of grid-connected inverter under weak grid by decoupling phase-lock loop and grid impedance," *IEEE Trans. Ind. Electron.*, vol. 69, no. 7, pp. 7040–7053, Jul. 2022.

[16] X. Lin, R. Yu, J. Yu, and H. Wen, "Constant coupling effect-based PLL for synchronization stability enhancement of grid-connected converter under weak grids," *IEEE Trans. Ind. Electron.*, vol. 70, no. 11, pp. 11310–11323, Nov. 2023.

[17] D. Zhu, S. Zhou, X. Zou, Y. Kang, and K. Zou, "Small-signal disturbance compensation control for LCL-type grid-connected converter in weak grid," *IEEE Trans. Ind. Appl.*, vol. 56, no. 3, pp. 2852–2861, May/Jun. 2020.

[18] X. Zhang, M. Li, and D. Xu, "PCC voltage perturbation path analysis and compensation for grid-connected voltage-source converter under weak grid," *IEEE Trans. Ind. Electron.*, vol. 68, no. 12, pp. 12331–12339, Dec. 2021.

[19] Z. Xie, Y. Chen, W. Wu, W. Gong, and J. M. Guerrero, "Stability enhancing voltage feed-forward inverter control method to reduce the effects of phase-locked loop and grid impedance," *IEEE Trans. Emerg. Sel. Topics Power Electron.*, vol. 9, no. 3, pp. 3000–3009, Jun. 2021.

[20] Y. Xia, M. Yu, X. Wang, and W. Wei, “Describing function method based power oscillation analysis of LCL-filtered single-stage PV generators connected to weak grid,” *IEEE Trans. Power Electron.*, vol. 34, no. 9, pp. 8724–8738, Sep. 2019.

[21] W. Liu, X. Xie, J. Shair, and X. Li, “A nearly decoupled admittance model for grid-tied VSCs under variable operating conditions,” *IEEE Trans. Power Electron.*, vol. 35, no. 9, pp. 9380–9389, Sep. 2020.

[22] W. Wu et al., “Sequence impedance modeling and stability comparative analysis of voltage-controlled VSGs and current-controlled VSGs,” *IEEE Trans. Ind. Electron.*, vol. 66, no. 8, pp. 6460–6472, Aug. 2019.

[23] M. Cespedes, L. Xing, and J. Sun, “Constant-power load system stabilization by passive damping,” *IEEE Trans. Power Electron.*, vol. 26, no. 7, pp. 1832–1836, Jul. 2011.

[24] H. Liu, X. Xie, X. Gao, H. Liu, and Y. Li, “Stability analysis of SSR in multiple wind farms connected to series-compensated systems using impedance network model,” *IEEE Trans. Power Syst.*, vol. 33, no. 3, pp. 3118–3128, May 2018.

[25] X. Wang and F. Blaabjerg, “Harmonic stability in power electronic-based power systems: Concept, modeling, and analysis,” *IEEE Trans. Smart Grid*, vol. 10, no. 3, pp. 2858–2870, May 2019.

[26] P. S. Kundur and O. P. Malik, *Power System Stability and Control*. New York, NY, USA: McGraw-Hill, 2022.

[27] N. Hatziargyriou et al., “Stability definitions and characterization of dynamic behavior in systems with high penetration of power electronic interfaced technologies,” IEEE PES Tech. Rep. PES-TR77, 2020.

[28] J. Sun, “Impedance-based stability criterion for grid-connected inverters,” *IEEE Trans. Power Electron.*, vol. 26, no. 11, pp. 3075–3078, Nov. 2011.

[29] W. Rui, S. Qiuye, Z. Pinjia, G. Yonghao, Q. Dehao, and W. Peng, “Reduced-order transfer function model of the droop-controlled inverter via Jordan continued-fraction expansion,” *IEEE Trans. Energy Convers.*, vol. 35, no. 3, pp. 1585–1595, Sep. 2020.

[30] Z. Xie et al., “Modeling and control parameters design for grid-connected inverter system considering the effect of PLL and grid impedance,” *IEEE Access*, vol. 8, pp. 40474–40484, 2020.

[31] S.-K. Chung, “A phase tracking system for three phase utility interface inverters,” *IEEE Trans. Power Electron.*, vol. 15, no. 3, pp. 431–438, May 2000.

[32] S. Ren, M. Chen, H. Cai, and C. Hu, “A proposed neutral-point voltage balancing method for three-phase three-level t-type inverter under non-unity power factor,” in *Proc. IEEE 13th Int. Symp. Power Electron. Distrib. Gener. Syst.*, 2022, pp. 1–6.

[33] D. Yang, X. Wang, F. Liu, K. Xin, Y. Liu, and F. Blaabjerg, “Symmetrical PLL for SISO impedance modeling and enhanced stability in weak grids,” *IEEE Trans. Power Electron.*, vol. 35, no. 2, pp. 1473–1483, Feb. 2020.

[34] M. Berg, A. Aapro, R. Luhtala, and T. Messo, “Small-signal analysis of photovoltaic inverter with impedance-compensated phase-locked loop in weak grid,” *IEEE Trans. Energy Convers.*, vol. 35, no. 1, pp. 347–355, Mar. 2020.

[35] M. F. M. Arani and Y. A.-R. I. Mohamed, “Analysis and performance enhancement of vector-controlled VSC in HVDC links connected to very weak grids,” *IEEE Trans. Power Syst.*, vol. 32, no. 1, pp. 684–693, Jan. 2017.

[36] F. Cecati, R. Zhu, S. Pugliese, M. Liserre, and X. Wang, “State feedback reshaping control of voltage source converter,” *IEEE Trans. Power Electron.*, vol. 37, no. 12, pp. 14280–14293, Dec. 2022.

[37] Z. Zhang, P. Wang, P. Jiang, F. Gao, L. Fu, and Z. Liu, “Robust control method of grid-connected inverters with enhanced current quality while connected to a weak power grid,” *IEEE Trans. Power Electron.*, vol. 37, no. 6, pp. 7263–7274, Jun. 2022.

[38] J. Fang, X. Li, H. Li, and Y. Tang, “Stability improvement for three-phase grid-connected converters through impedance reshaping in quadrature-axis,” *IEEE Trans. Power Electron.*, vol. 33, no. 10, pp. 8365–8375, Oct. 2018.

[39] X. Chen, Y. Zhang, S. Wang, J. Chen, and C. Gong, “Impedance-phased dynamic control method for grid-connected inverters in a weak grid,” *IEEE Trans. Power Electron.*, vol. 32, no. 1, pp. 274–283, Jan. 2017.

[40] X. Wang, Y. W. Li, F. Blaabjerg, and P. C. Loh, “Virtual-impedance-based control for voltage-source and current-source converters,” *IEEE Trans. Power Electron.*, vol. 30, no. 12, pp. 7019–7037, Dec. 2015.

[41] W. Li, X. Ruan, D. Pan, and X. Wang, “Full-feedforward schemes of grid voltages for a three-phase LCL-type grid-connected inverter,” *IEEE Trans. Ind. Electron.*, vol. 60, no. 6, pp. 2237–2250, Jun. 2013.

[42] R. Wang, X. Yu, Q. Sun, D. Li, Y. Gui, and P. Wang, “The integrated reference region analysis for parallel DFIGs’ interfacing inductors,” *IEEE Trans. Power Electron.*, vol. 39, no. 6, pp. 7632–7642, Jun. 2024.

Zhengqi Sui received the B.S. degree in automation in 2021 from Northeastern University, Shenyang, China, where he is currently working toward the Ph.D. degree in electrical engineering.

His research interests include impedance characteristic analysis and stability analysis of the inverter grid connected system.

Qiuye Sun (Senior Member, IEEE) received the Ph.D. degree in control theory and control engineering from Northeastern University, Shenyang, China, in 2007.

He is currently a Full Professor with Northeastern University and obtained Special Government Allowances from the State Council in China. His current research interests include optimization analysis technology of power distribution network, network control of energy Internet, integrated energy systems, and microgrids.

Rui Wang (Senior Member, IEEE) received the B.S. degree in electrical engineering and automation and the Ph.D. degree in power electronics and power drive from Northeastern University, Shenyang, China, in 2016 and 2021, respectively.

He is currently an Associate Professor with Northeastern University. He has authored or coauthored more than 50 papers, and authorized more than 20 invention patents. His research interests include collaborative optimization of distributed generation and its stability analysis.

Dashuang Li (Student Member, IEEE) received the B.S. and M.Sc. degrees in electrical engineering, in 2013 and 2015, respectively, from Northeastern University, Shenyang, China, where he is currently working toward the Ph.D. degree in electrical engineering.

His research interests include collaborative optimization and stability analysis of distributed generation.

Peng Wang (Fellow, IEEE) received the B.Sc. degree in electronic engineering from Xian Jiaotong University, Xian, China, in 1978, the M.Sc. degree in electronic engineering from the Taiyuan University of Technology, Taiyuan, China, in 1987, and the M.Sc. and Ph.D. degrees in electrical engineering from the University of Saskatchewan, Saskatoon, SK, Canada, in 1995 and 1998, respectively.

He is currently a Full Professor with the School of Electrical and Automation Engineering, Nanjing Normal University, Nanjing, China. His current research interests include power system planning and operation, renewable energy planning, solar or electricity conversion system, and power system reliability analysis.

Dr. Wang is an Associate Editor or Guest Editor-in Chief for or of the IEEE Transactions on Smart Grid, IEEE Transactions on Power Delivery, *Journal of Modern Power Systems and Clean Energy*, and *CSEE Journal of Power and Energy Systems*.